

# Performance of wall-modeled LES with boundary-layer-conforming grids for external aerodynamics

Adrián Lozano-Durán\*

*Massachusetts Institute of Technology, Massachusetts 02139, USA*

Sanjeeb T. Bose†

*Stanford University, Stanford, California 94305, USA*

*Cascade Technologies, Inc., Palo Alto, California 94303, USA*

Parviz Moin‡

*Stanford University, Stanford, California 94305, USA*

We investigate the error scaling and computational cost of wall-modeled large-eddy simulation (WMLES) for external aerodynamic applications. The NASA Juncture Flow is used as representative of an aircraft with trailing-edge smooth-body separation. Two gridding strategies are examined: i) constant-size grid, in which the near-wall grid size has a constant value and ii) boundary-layer-conforming grid (BL-conforming grid), in which the grid size varies to accommodate the growth of the boundary-layer thickness. Our results are accompanied by a theoretical analysis of the cost and expected error scaling for the mean pressure coefficient ( $C_p$ ) and mean velocity profiles. The prediction of  $C_p$  is within less than 5% error for all the grids studied, even when the boundary layers are marginally resolved. The high accuracy in the prediction of  $C_p$  is attributed to the outer-layer nature of the mean pressure in attached flows. The errors in the predicted mean velocity profiles exhibit a large variability depending on the location considered, namely, fuselage, wing-body juncture, or separated trailing-edge. WMLES performs as expected in regions where the flow resembles a zero-pressure-gradient turbulent boundary layer such as the fuselage ( $< 5\%$  error). However, there is a decline in accuracy of WMLES predictions of mean velocities in the vicinity of wing-body junctions and, more acutely, in separated zones. The impact of the propagation of errors from the underresolved wing leading-edge is also investigated. It is shown that BL-conforming grids enable a higher accuracy in wing-body junctions and separated regions due to the more effective distribution of grid points, which in turn diminishes the streamwise propagation of errors.

---

\*Draper Assistant Professor, Department of Aeronautics and Astronautics, Massachusetts Institute of Technology, AIAA Senior Member (Corresponding Author).

†Chief Technology Officer of Cascade Technologies, Inc. and Center for Turbulence Research, Stanford University. Member AIAA.

‡Franklin P. and Caroline M. Johnson Professor, Center for Turbulence Research. Fellow AIAA.

## I. Introduction

THE use of computational fluid dynamics (CFD) for external aerodynamic applications has been a key tool for aircraft design in the modern aerospace industry [1–3]. CFD methodologies with increasing functionality and performance have greatly improved our understanding and predictive capabilities of complex flows. These improvements suggest that Certification by Analysis (CbA) –prediction of the aerodynamic quantities of interest by numerical simulations [4] may soon be a reality. CbA is expected to reduce the number of wind tunnel tests, reducing both the turnover time and cost of the design cycle [5]. However, flow predictions from the state-of-the-art CFD solvers are still unable to comply with the stringent accuracy requirements and computational efficiency demanded by the industry [6]. These limitations are imposed, largely, by the defiant ubiquity of turbulence. In the present work, we investigate the cost and performance of wall-modeled large-eddy simulation (WMLES) to predict quantities of interest in the NASA Juncture Flow Experiment [7].

One of the major challenges in CFD is the prediction of corner flow and smooth-body separation [8, 9]. In the latter, the loss of momentum across the boundary layer eventually leads to flow detachment, which can significantly affect the performance of an aircraft wing. In wing-fuselage junctions, the flow is often observed to separate in the corner region near the wing trailing-edge. This is also the case at the angles of attack (AoA) typically encountered during take-off and landing [10]. Current turbulence models, such as those utilized in Reynolds-averaged Navier-Stokes CFD (RANS), have performed poorly in predicting the onset and extent of the three-dimensional separated flow in wing-fuselage junctions [11]. These deficiencies have been exposed in previous AIAA Drag Prediction Workshops [12], where large variations in the prediction of separation, skin friction, and pressure were documented in the corner-flow region near the wing trailing-edge.

To advance the state-of-the-art of CFD in realistic separated flows, NASA has developed a validation experiment for a generic full-span wing-fuselage junction model at subsonic conditions: the NASA Juncture Flow Experiment. The reader is referred to Rumsey et al. [7] for a summary of the history and goals of the experiment [see also 13, 14]. The geometry and flow conditions are designed to trigger flow separation in the trailing edge corner of the wing, with recirculation bubbles varying in size with the AoA. The model is a full-span wing-fuselage body that was configured with truncated DLR-F6 wings, both with and without leading-edge horn at the wing root. The model has been tested at a chord Reynolds number of 2.4 million, and AoAs ranging from -10 degrees to +10 degrees in the Langley 14- by 22-foot Subsonic Tunnel. An overview of the experimental measurements can be found in Kegerise et al. [15]. The main aspects of the planning and execution of the project are discussed by Rumsey [16], along with details about the CFD and experimental teams.

To date, most CFD efforts on the NASA Juncture Flow Experiment have been conducted using RANS or hybrid-RANS solvers. Lee et al. [17] performed the first CFD analysis to aid the NASA Juncture Flow committee in selecting the wing configuration for the final experiment. Lee et al. [18] presented a preliminary CFD study of the near wing-body

juncture region to evaluate the best practices in simulating wind tunnel effects. Rumsey et al. [7] used NASA’s FUN3D[19–21] to investigate the ability of RANS-based CFD solvers to predict the flow details leading up to separation. The study comprised different RANS turbulence models such as a linear eddy viscosity one-equation model, a nonlinear version of the same model, and a full second-moment seven-equation model. Rumsey et al. [7] also performed a grid sensitivity analysis and CFD uncertainty quantification. Comparisons between CFD simulations and the wind tunnel experimental results have been recently documented by Lee and Pulliam [22].

WMLES of the NASA Juncture Flow has been less thoroughly investigated, despite NASA’s recognition of WMLES as a critical pacing item for “developing a visionary CFD capability required by the notional year 2030”. According to NASA’s recent CFD Vision 2030 report [6], hybrid RANS/LES [23, 24] and WMLES [25] are identified as the most viable approaches for predicting realistic flows at high Reynolds numbers in external aerodynamics. Previous attempts of WMLES of the NASA Juncture Flow include the works by Iyer and Malik [26], Ghate et al. [27], and Lozano-Durán et al. [28, 29]. These studies highlighted the capabilities of WMLES to predict wall pressure, velocity and Reynolds stresses, especially compared with RANS-based methodologies. Nonetheless, it was noted that WMLES is still far from providing the robustness and stringent accuracy required for CbA, especially in the separated regions and wing-fuselage juncture.

The goal of this study is to systematically quantify the errors in the mean quantities of interest in the NASA Juncture Flow using WMLES. Several strategies have been proposed to model the near-wall region in WMLES, and comprehensive reviews can be found in Piomelli and Balaras [30], Cabot and Moin [31], Spalart [24], Larsson et al. [32], and the most recent review by Bose and Park [25]. We follow the wall-flux modeling approach (or approximate boundary conditions modeling), where the no-slip and thermal wall boundary conditions are replaced with stress and heat flux boundary conditions provided by the wall model. This category of wall models utilizes the LES solution at a given location in the LES domain as input, and returns the wall-fluxes needed by the LES solver. Examples of the most popular and well-known approaches are those computing the wall stress using either the law of the wall [33–35] or the full/simplified RANS equations [36–44]. We will not attempt here to devise improvements that alleviate current modeling limitations. The interested reader may refer to Lozano-Durán and Bae [45] for new modeling venues in WMLES applied to the NASA Juncture Flow.

This work is organized as follows. The flow setup, mathematical modeling, and numerical approach are presented in Section II. The strategies for grid generation are discussed in Section III along with the computational cost of WMLES. In Section IV, we introduce the theoretical analysis for the error scaling. WMLES of the NASA Juncture Flow is presented in Section V, which includes predictions for mean velocity profiles and Reynolds stresses for three different locations on the aircraft: the upstream region of the fuselage, the wing-body juncture, and the wing-body juncture close to the trailing edge. We also discuss the prediction of the mean surface pressure coefficient at different spanwise locations over the wing. Finally, conclusions are offered in Section VI.



**Fig. 1** Experimental setup of the NASA Juncture Flow at NASA Langley 14- by 22-Foot Subsonic Wind Tunnel.

## II. Numerical Methods

### A. Flow conditions and computational setup

We use the NASA Juncture Flow geometry with a wing based on the DLR-F6 and a leading-edge horn to mitigate the effect of the horseshoe vortex over the wing-fuselage juncture (figure 1). The model wingspan is nominally 3397.2 mm, the fuselage length is 4839.2 mm, and the crank chord (chord length at the Yehudi break) is  $L = 557.1$  mm. The frame of reference is such that the fuselage nose is located at  $x = 0$ , the  $x$ -axis is aligned with the fuselage centerline, the  $y$ -axis denotes spanwise direction, and the  $z$ -axis is the vertical direction (away from the fuselage upstream of the wing). The associated instantaneous velocities are denoted by  $u$ ,  $v$ , and  $w$ , and occasionally by  $u_1$ ,  $u_2$ , and  $u_3$ . The wing leading-edge horn meets the fuselage at  $x = 1925$  mm, and the wing root trailing-edge is located at  $x = 2961.9$  mm.

In the experiment, the model was tripped near the front of the fuselage and on the upper and lower surfaces of both wings. In our case, preliminary calculations showed that tripping was also necessary to trigger the transition to turbulence over the wing. Hence, the geometry of the wing was modified by displacing in the  $z$  direction a line of surface mesh points close to the leading edge by 1 mm along the suction side of the wing, and by -1 mm along the pressure side. The tripping lines follow approximately the location of the tripping dots used in the experimental setup for the left wing (lower surface  $x = (4144 - y)/2.082$ ; upper surface  $x = (3775 - y)/1.975$  for  $y < -362$  and  $x = (2847 - y)/1.532$  for  $y > -362$ ). Tripping using dots mimicking the experimental setup was also tested. It was found that the results over the wing-body juncture show little sensitivity to the tripping due to the presence of the incoming boundary layer from the fuselage. No tripping was needed on the fuselage, which naturally transitioned from laminar to turbulence.

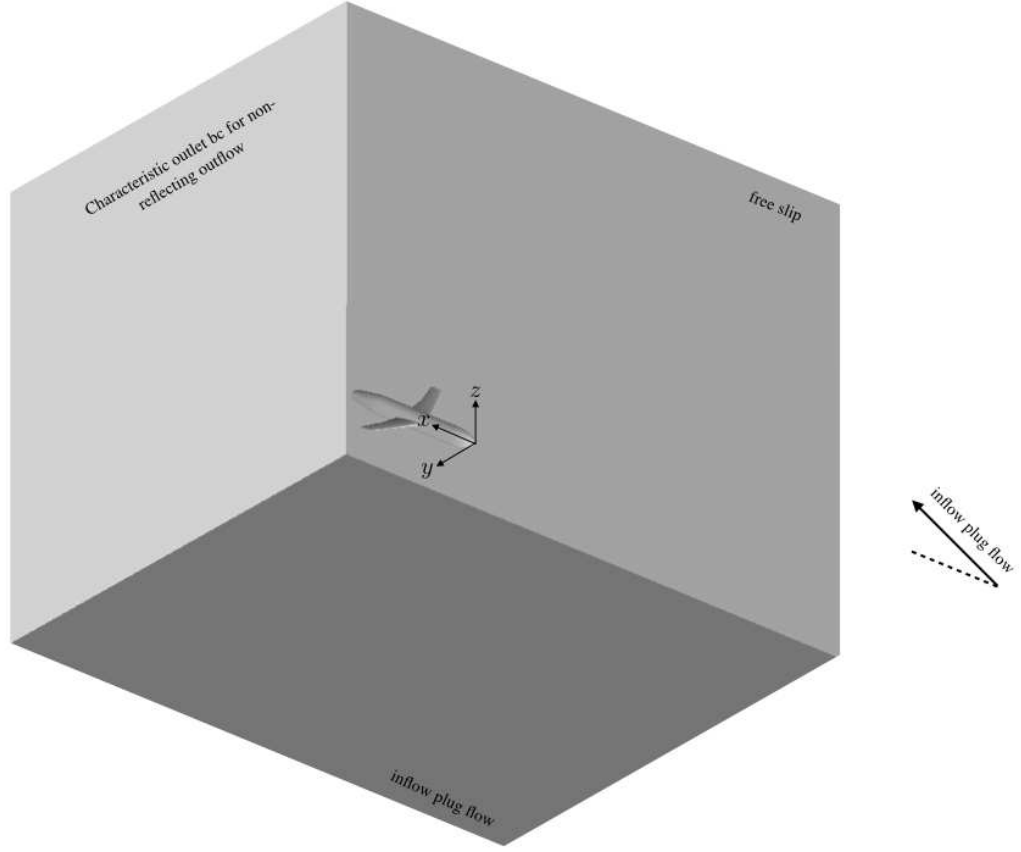


**Fig. 2 Computational domain and NASA Juncture Flow model.**

In the wind tunnel, the model was mounted on a sting aligned with the fuselage axis. The sting was attached to a mast that emerged from the wind tunnel floor. Here, all calculations are performed in free air conditions, and the sting and mast are ignored. The computational setup is such that the dimensions of the domain are about five times the length of the fuselage in the three directions (figure 2). The Reynolds number is  $Re = LU_\infty/\nu = 2.4$  million based on the crank chord length  $L$ , freestream velocity  $U_\infty$ , and the kinematic viscosity  $\nu$ . The freestream Mach number is  $Ma = 0.189$ , the freestream temperature is  $T = 288.84$  K, and the dynamic pressure is 2476 Pa. We impose a uniform plug flow as inflow boundary condition in the front and bottom boundaries of the domain. The Navier–Stokes characteristic boundary condition for subsonic non-reflecting outflow is imposed at the outflow and top boundaries [46] and free-slip is used at the lateral boundaries. At the aircraft wall, we impose Neumann boundary condition with the shear stress provided by the wall model as described in Section II.B.

## B. Numerical methods, subgrid-scale model and wall model

The simulations are conducted with the high-fidelity solver charLES developed by Cascade Technologies, Inc [47, 48]. The code integrates the compressible LES equations using a kinetic-energy conserving, second-order accurate, finite volume method. The numerical discretization relies on a flux formulation which is approximately entropy preserving in the inviscid limit, thereby limiting the amount of numerical dissipation added into the calculation. The time integration is performed with a third-order Runge-Kutta explicit method. The SGS model is the dynamic Smagorinsky model [49] with the modification by Lilly [50].

We utilize a wall model to overcome the restrictive grid-resolution requirements imposed by the small-scale motions in the vicinity of the walls. The no-slip boundary condition at the walls is replaced by a wall-stress boundary condition. The walls are assumed adiabatic and the wall stress is obtained by an algebraic equilibrium wall model derived from the integration of the one-dimensional stress model along the wall-normal direction [33, 35],

$$u_{||}^+(y_{\perp}^+) = \begin{cases} y_{\perp}^+ + a_1 (y_{\perp}^+)^2 & \text{for } y_{\perp}^+ < 23, \\ \frac{1}{\kappa} \ln y_{\perp}^+ + B & \text{otherwise} \end{cases} \quad (1)$$

where  $u_{||}$  is the model wall-parallel velocity,  $y_{\perp}$  is the wall-normal direction to the aircraft surface,  $\kappa = 0.41$  is the Kármán constant,  $B = 5.2$  is the intercept constant, and  $a_1$  is computed to ensure  $C^1$  continuity. The superscript  $+$  denotes inner units defined in terms of wall friction velocity ( $u_{\tau}$ ) and  $\nu$ . The matching location for the wall model is the first off-wall cell center of the LES grid, denoted by  $h_w$ , at which  $u_{||}$  equals the wall-parallel velocity of the LES solution. No temporal filtering or other treatments were used for the LES velocity at the matching location.

## III. Grid strategies and computational cost

### A. Grid generation: constant-size grid vs. boundary-layer-conforming grid

The mesh generation is based on a Voronoi hexagonal close-packed point-seeding method. We examine two strategies to distribute the cell centroids of the control volumes as illustrated in Figure 3:

- (i) Constant-size grid. In the first approach, we set the grid size in the vicinity of the aircraft surface to be roughly constant and isotropic  $\Delta \approx \Delta_x \approx \Delta_y \approx \Delta_z$ , where  $\Delta_x$ ,  $\Delta_y$  and  $\Delta_z$  are the characteristic grid sizes in  $x$ ,  $y$ , and  $z$  directions, respectively. Starting from the wall and building up the grid, the number of cell layers with size  $\Delta$  is specified to be five. We set the farfield grid resolution,  $\Delta_{\text{far}} \gg \Delta$ , and create additional layers with varying grid size to blend the near-wall grid with the farfield grid. The meshes are constructed using a Voronoi diagram and ten iterations of Lloyd's algorithm to smooth the transition between layers with different grid resolutions. The concept is illustrated in Figure 3(a) for a flat plate, while Figure 4(a) shows the actual grid structure in the NASA Juncture Flow for  $\Delta = 2$  mm and  $\Delta_{\text{far}} = 200$  mm. This grid-generation approach is algorithmically simple and efficient.

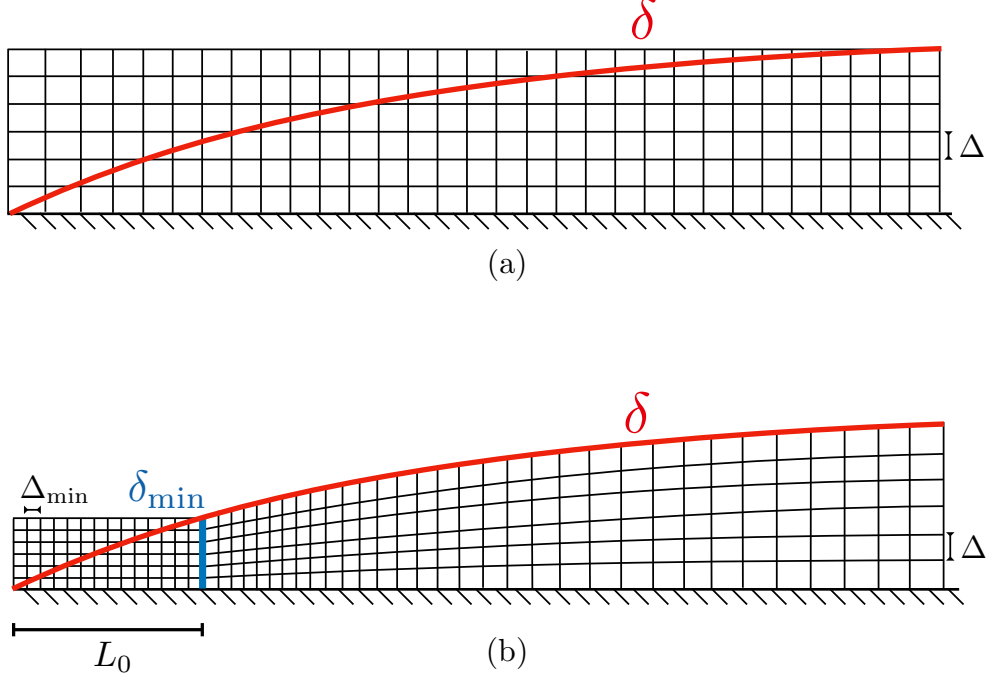


**Fig. 3 Schematic of (a) constant-size grid and (b) BL-conforming grid for a ZPGTBL.**

However, it is agnostic to details of the actual flow such as wake/shear regions and boundary-layer growth. This implies that flow regions close to the fuselage nose and wing leading-edge are underresolved (less than one point per boundary-layer thickness), whereas the wing trailing edge and the downstream-fuselage regions are seeded with up to hundreds of points per boundary-layer thickness. The gridding strategy (ii) aims at providing a more equitable distribution of grid points.

- (ii) Boundary-layer-conforming grid. In the second gridding strategy, we account for the actual growth of the turbulent boundary layers, denoted by  $\delta$ , by seeding the control volumes consistently with its growth. We refer to this approach as boundary-layer-conforming grid (BL-conforming grid). The method necessitates two parameters. The first one is the number of points per boundary-layer thickness,  $N_{bl}$ , such that  $\Delta_x \approx \Delta_y \approx \Delta_z \approx \Delta \approx \delta/N_{bl}$  is a function of space. The second parameter is less often discussed in the literature and is the minimum local Reynolds number that we are willing to marginally resolve in the flow,  $Re_{\Delta}^{\min} \equiv \Delta_{\min} U_{\infty}/\nu$ , where  $\Delta_{\min}$  is the smallest grid resolution permitted. This is a necessary constraint as  $\delta \rightarrow 0$  at the leading edge of the body, which would impose a large burden on the number of points required to cover this region. Hence, the grid resolution is kept constant and equal to  $\Delta_{\min}$  at those regions where the boundary-layer thickness is below  $\delta_{\min} = N_{bl}\Delta_{\min}$  (see Figure 3(b)). We also impose a geometric constraint on the grid size such that  $\Delta$  must be smaller than the local radius of curvature  $R$  of the surface. The grid is then constructed by seeding points within the boundary layer with

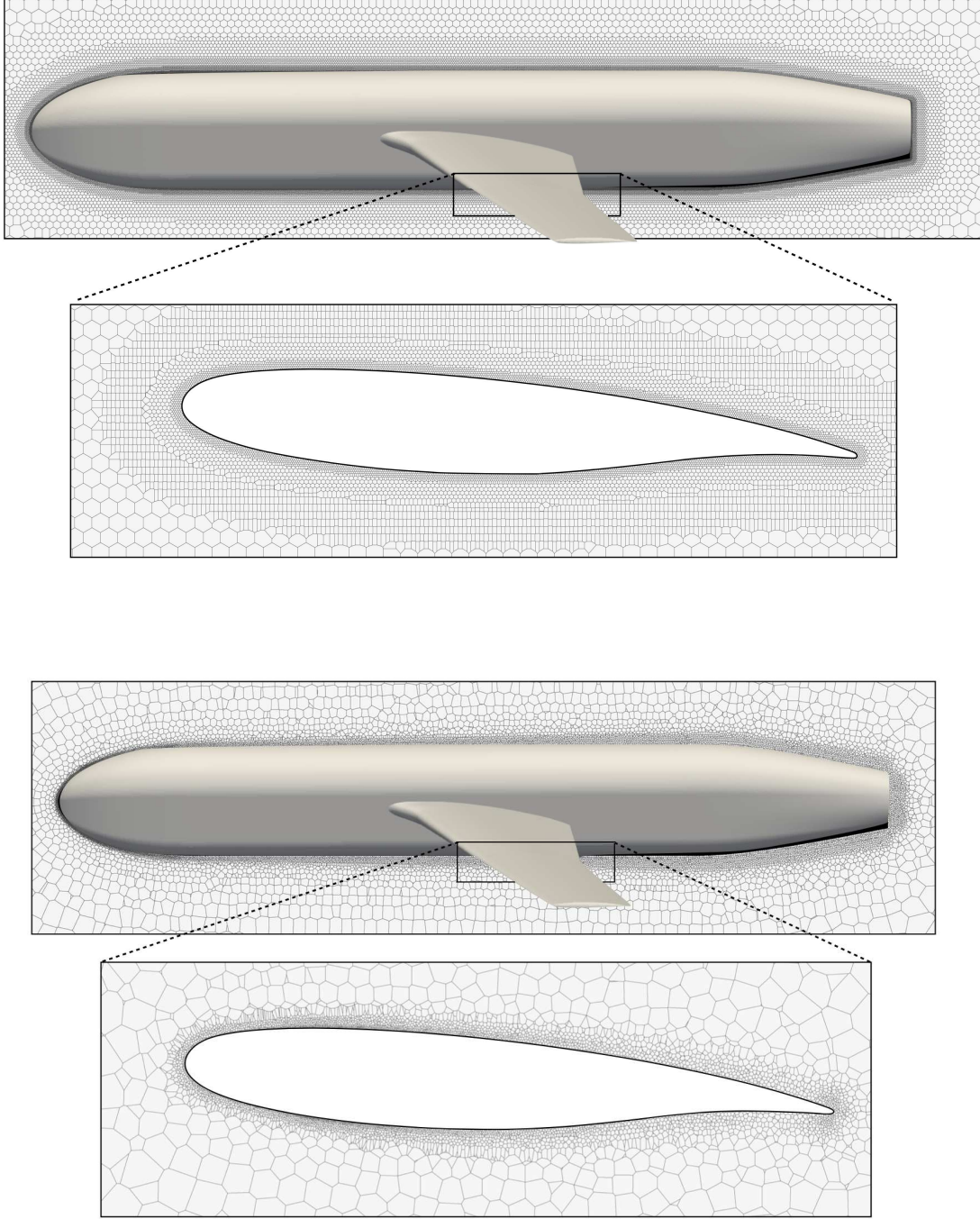


**Fig. 4** Visualization of Voronoi control volumes for (top) constant-size grid following strategy i) with  $\Delta = 2$  mm and  $\Delta_{\text{far}} = 200$  mm and (bottom) boundary-layer-conforming grid following strategy ii) with  $N_{\text{bl}} = 5$  and  $Re_{\Delta}^{\text{min}} = 2.8 \times 10^3$ .



space-varying grid size

$$\Delta(x, y, z) \approx \min \left[ \max \left( \frac{\gamma \delta}{N_{bl}}, \frac{Re_{\Delta}^{\min} \gamma}{U_{\infty}} \right), \beta R \right], \quad (2)$$

where  $\gamma = 1.2$  is a correction factor for  $\delta$  to ensure that the near-wall grid contains the instantaneous boundary layer, and  $\beta = 1/2$ . Note that the grid is still locally isotropic and the characteristic size of the control volumes is  $\Delta \approx \delta/N_{bl}$  in the three spatial directions. Figure 4(b) shows the structure of a BL-conforming grid in the NASA Juncture Flow with  $N_{bl} = 5$  and  $Re_{\Delta}^{\min} = 2.8 \times 10^3$ . Additional control volumes of increasing size are created to blend the near-wall grid with the farfield grid of size  $\Delta_{far} = 200$  mm.

The gridding approach above requires an estimation of the boundary-layer thickness at each location of the aircraft surface. Given that boundary layers originate from viscous effects, the method proposed here is based on measuring the deviation of the viscous solution from a reference inviscid flow. This is achieved by conducting two simulations: one WMLES, whose velocity is denoted as  $\mathbf{u}$ , and one inviscid simulation (no SGS model and free-slip at the wall), with velocity denoted by  $\mathbf{u}_I$ . The grid generation for the two simulations follows strategy (i) with  $\Delta = 2$  mm. Boundary layers at the leading edge with thickness below 2 mm are estimated by extrapolating the solution using a power law. Two examples of mean velocity profiles for  $\mathbf{u}$  and  $\mathbf{u}_I$  are shown in Figures 5(a) and (b). The three-dimensional surface representing the boundary layer edge  $S_{bl}$  is identified as the loci of

$$S_{bl} \equiv \left\{ (x, y, z) : \frac{||\langle \mathbf{u}_I(x, y, z) \rangle - \langle \mathbf{u}(x, y, z) \rangle||}{||\langle \mathbf{u}_I(x, y, z) \rangle||} = 0.01 \right\}, \quad (3)$$

where  $\langle \cdot \rangle$  denotes time-average. Finally, at each point of the aircraft surface  $(x_a, y_a, z_a)$ , the boundary-layer thickness  $\delta$  is defined as the minimum spherical distance between  $\mathbf{x}_a = (x_a, y_a, z_a)$  and  $\mathbf{x} = (x, y, z) \in S_{bl}$ ,

$$\delta(\mathbf{x}_a) \equiv ||\mathbf{x}_a - \mathbf{x}||_{\min}, \quad \forall \mathbf{x} \in S_{bl}. \quad (4)$$

The boundary-layer thickness for the NASA Juncture Flow at  $Re = 2.4M$  and  $AoA=5$  is shown in Figure 5(c). The values of  $\delta$  range from  $\sim 0$  mm at the leading edge of the wing to  $\sim 30$  mm at the trailing edge of the wing. Thicker boundary layers above 50 mm are found in the downstream region of the fuselage. Equation (3) might be interpreted as the definition of a turbulent/nonturbulent interface, although it also applies to laminar regions. Other approaches for defining  $S_{bl}$ , such as isosurfaces of Q-criterion, were also explored and combined with Eq. (4) to obtained a boundary-layer interface. The results were similar to the ones reported in Figure 5(c), probably because the present flow is dominated by attached boundary layers with very mild separations. In these cases, Eq. (3) stands as a reasonable indicator of the regions influenced by viscous effects for the purpose of generating BL-conforming grids. It is worth mentioning that other methods for estimating  $\delta$  are available in the literature [e.g. 51–56]. They feature varying degrees of complexity and generalizability and also may offer a sensible estimation of  $\delta$  when properly conditioned to complex

geometries.

## B. Required number of grid points and time steps

We estimate the number of grid points (or control volumes) to conduct WMLES of the NASA Juncture Flow as a function of the Reynolds number ( $Re$ ), the number of points per boundary-layer thickness ( $N_{bl}$ ) and the minimum grid Reynolds number ( $Re_{\Delta}^{\min}$ ). We assume the gridding strategy (ii) and utilize the Juncture Flow geometry. The boundary-layer thickness was obtained following the procedure in Section III.A. The total number of points,  $N_{\text{points}}$ , to grid the boundary layer spanning the surface area of the aircraft  $S_a$  is

$$N_{\text{points}} = \int_0^{\delta} \iint_{S_a} \frac{1}{\Delta(x_{||}, z_{||})^3} dx_{||} dz_{||} dy_{\perp} = \iint_{S_a} \frac{N_{bl}}{\Delta(x_{||}, z_{||})^2} dx_{||} dz_{||}, \quad (5)$$

where  $x_{||}$  and  $z_{||}$  are the local aircraft wall-parallel directions, and  $y_{\perp}$  is the local wall-normal direction. Equation (5) only accounts for the points within the boundary layer and neglects the points in the farfield and the transition grid in between. However, the latter are usually smaller than the number of points in the vicinity of the aircraft wall. Note that all the cost estimates of WMLES are predicated upon Eq. (5) with BL-conforming grids [see 23, 57–59]; yet, to the best of our knowledge WMLES of an aircraft geometry has never been conducted using a true BL-conforming grids until the present work. Equation (5) is integrated numerically and the results are shown in Figure 6. The cost map in Figure 6(a) contains  $\log_{10}(N_{\text{points}})$  as a function of  $N_{bl}$  and  $Re_{\Delta}^{\min}$ . The accuracy of the solution is expected to improve for increasing values of  $N_{bl}$  (i.e., higher energy content resolved by the LES grid), and decrease with increasing  $Re_{\Delta}^{\min}$  (i.e., worse leading-edge resolution).  $Re_{\Delta}^{\min}$  can also be understood as the largest subgrid boundary-layer that can be resolved by the LES grid using  $N_{bl}$  points. Figure 6(b) provides an illustration of the subgrid-boundary-layer region for  $Re_{\Delta}^{\min} < 10^4$ , which is confined to a small region (less than 10% of the chord) at the leading edge of the wing.

The scaling properties of Eq. (5) can be unfolded by considering a wall-attached, zero-pressure gradient flat-plate turbulent boundary layer (ZPGTBL) with  $\delta \sim (x - x_e)[(x - x_e)U_{\infty}/\nu]^{-m}$ , where  $x_e$  is the streamwise distance to the leading edge and  $m \approx -1/7$  [60]. If we further assume that  $Re \gg Re_{\Delta}^{\min}$ , the number of control volumes can be shown to scale as

$$N_{\text{points}} \sim N_{bl}^{13/6} Re \left( Re_{\Delta}^{\min} \right)^{-5/6}, \quad (6)$$

which is also included in Figures 6(c) and (d) for reference. Equation (6) is the generalization of the WMLES cost scaling from previous works [23, 57–59] that explicitly accounts for  $N_{bl}$  and  $Re_{\Delta}^{\min}$  (see appendix A for the derivation). Additionally, the number of time steps to integrate the equations of motion for a time  $T$  is

$$N_{\text{steps}} = T/\Delta t \sim TU_{\infty}/\Delta_{\min} = \tilde{T} Re (Re_{\Delta}^{\min})^{-1}, \quad (7)$$

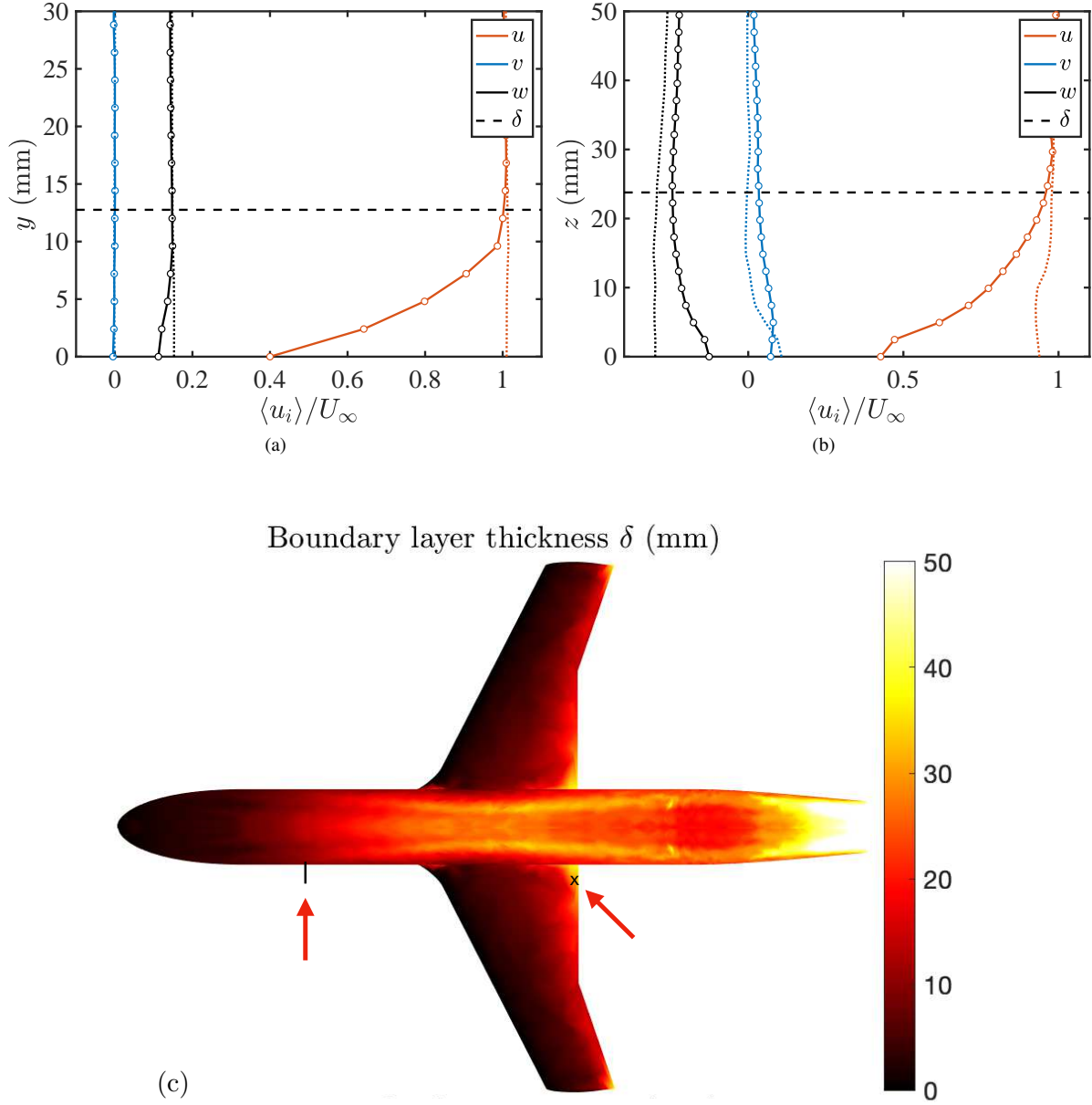


**Fig. 5** The three mean velocity components for  $\langle u \rangle$  (lines with symbols) and  $\langle u_I \rangle$  (dotted lines), and boundary layer height (dashed). The locations of the mean profiles are indicated in panel (c) by the solid line for panel (a) and the cross for panel (b). (c) Boundary-layer thickness (in millimeters) for the NASA Juncture Flow at AoA = 5 degrees and  $Re = 2.4 \times 10^6$ .

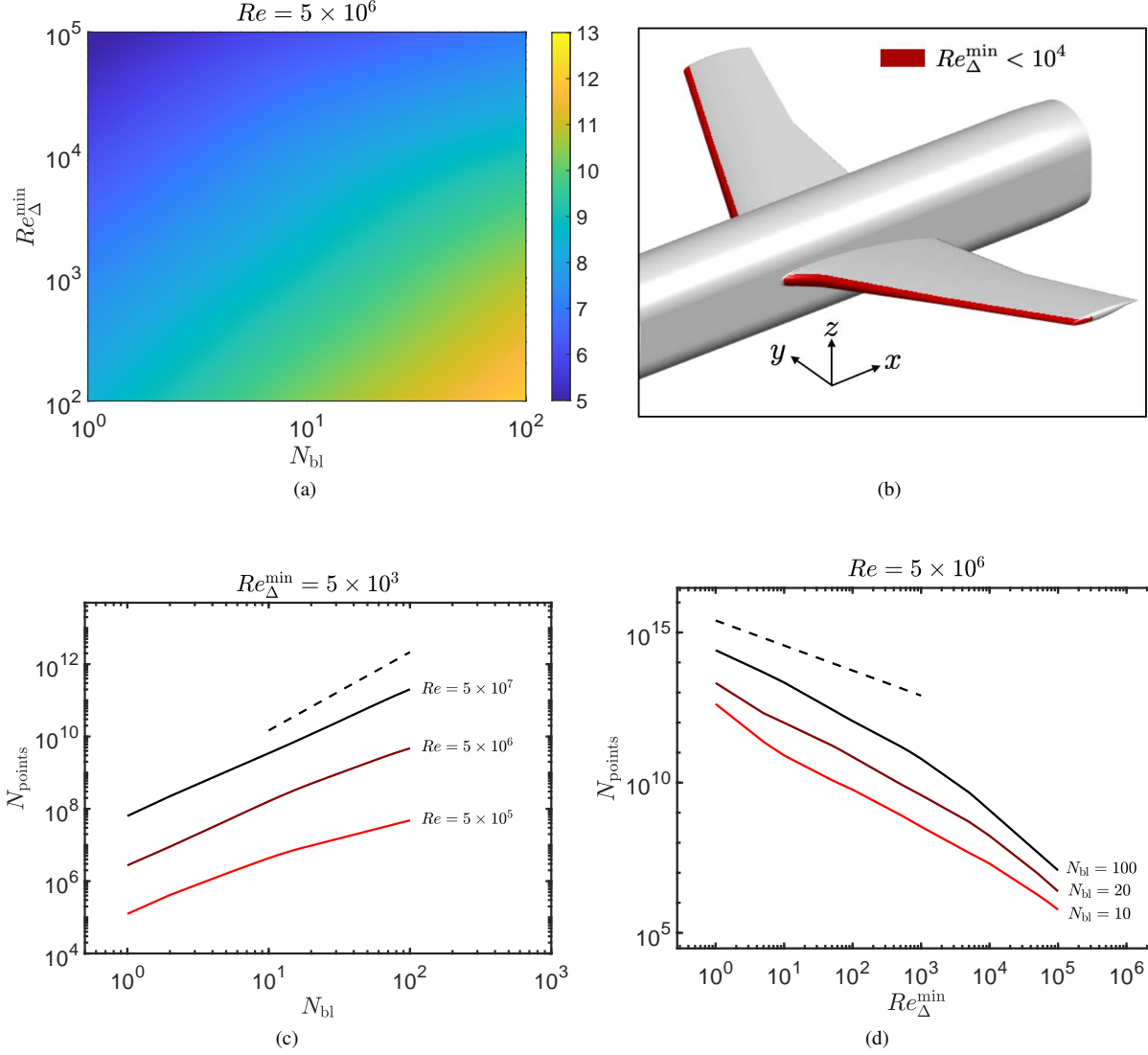


**Fig. 6** (a) Logarithm of the number of points ( $\log_{10} N_{\text{points}}$ ) required for WMLES of the NASA Juncture Flow geometry as a function of the number of grid points per boundary-layer thickness ( $N_{\text{bl}}$ ) and minimum grid Reynolds number ( $Re_{\Delta}^{\min}$ ) for  $Re = 5 \times 10^6$ . (b) Subgrid boundary-layer region (in red) for  $Re_{\Delta}^{\min} = 10^4$  at  $Re = 5 \times 10^6$ . Panels (c) and (d) are the number of grid points as a function of (c)  $N_{\text{bl}}$  and (d)  $Re_{\Delta}^{\min}$ . The dashed lines in panels (c) and (d) represent the power laws in Eq. (6).

where  $\Delta t$  is the time step,  $\tilde{T} = TU_\infty/L$  is the flow-through time with respect to the crank chord, and we have assumed that the simulation is constrained by the convective time-step  $\Delta t \sim \Delta_{\min}/U_\infty$ . Equation (7) shows that both  $Re$  and  $Re_\Delta^{\min}$  (i.e., leading-edge resolution) are key contributors to the time-integration cost of WMLES. The total, space-time computational cost is given by  $N_c = C(N_{\text{points}} \cdot N_{\text{steps}})$ , where  $C$  is a machine/code-dependent function that converts  $N_{\text{points}} \cdot N_{\text{steps}}$  to core-hours.

The Reynolds number considered in Figure 6 is  $Re = 5 \times 10^6$ , which is representative of wind tunnel experiments. For an actual aircraft in flight conditions, the typical Reynolds number is  $Re \approx 5 \times 10^7$ , that would increase  $N_{\text{points}}$  by roughly a factor of ten due to the thinning of the boundary layers as seen in Eq. (6). More notably, Eq. (6) shows that the cost of WMLES with  $N_{\text{bl}}$  scales roughly as  $N_{\text{bl}}^{13/6} \approx N_{\text{bl}}^2$ , which becomes very computationally demanding even for moderate values of  $N_{\text{bl}}$ . The dependence of  $N_{\text{points}}$  on  $Re_\Delta^{\min}$  is milder, but values of  $Re_\Delta^{\min} < 10^3$  become rapidly unattainable. This reiterates the critical importance of establishing the range of admissible  $N_{\text{bl}}$  and  $Re_\Delta^{\min}$  to achieve the desired accuracy for a given quantity of interest. Additionally, different quantities of interest might not need to share the same grid requirements. For example, if  $N_{\text{bl}} \approx 5$  and  $Re_\Delta^{\min} \approx 10^4$  suffice to attain the desired accuracy in the quantities of interest at  $Re = 5 \times 10^6$ , then the required number of points is  $O(10)$  million, which can be currently simulated in hours using  $O(1000)$  CPU cores. However, if the desired accuracy for the quantities of interest is such that  $N_{\text{bl}} \approx 20$  and  $Re_\Delta^{\min} \approx 10^3$ , the number of grid points increases up to  $O(1000)$  million, which renders WMLES unfeasible as a routine tool in industry. Hence, the key to the success of WMLES as a design tool resides in the accuracy of the solution achieved as a function of  $N_{\text{bl}}$  and  $Re_\Delta^{\min}$ . This calls for a systematic error characterization of the quantities of interest, which is the objective of the following sections.

## IV. Error scaling of WMLES

### A. Error definition

The purpose of this section is to establish the expectations of the error scaling of WMLES in ZPGTBL. This error will serve as the baseline to determine whether WMLES is over- or under-performing in the NASA Juncture Flow calculations. The analysis is motivated by the fact that the solutions from WMLES are intrinsically grid-dependent, i.e. the grid size is an explicit variable of the governing equations. As such, WMLES should be framed as a convergence study and multiple computations are required in order to faithfully assess the quality of the results. This raises the fundamental question of what is the expected WMLES error as a function of the flow parameters and grid resolution. To tackle this problem, we follow the error-scaling methodology from Lozano-Durán and Bae [61]. Taking the experimental values ( $\mathbf{q}^{\text{exp}}$ ) as ground truth, the relative error in a quantity of interest  $\langle \mathbf{q} \rangle$  is defined as

$$\varepsilon_q \equiv \frac{||\langle \mathbf{q}^{\text{exp}} \rangle - \langle \mathbf{q} \rangle||_n}{||\langle \mathbf{q}^{\text{exp}} \rangle||_n} = f\left(\frac{\Delta}{\delta}, Re, Ma, \text{geometry}, \dots\right), \quad (8)$$

where  $\|\cdot\|_n$  is the  $L_2$ -norm over the vector components and spatial coordinates of  $\langle \mathbf{q} \rangle$ , and  $f$  is the error function that in general depends on the non-dimensional parameters of the problem and the geometry. For a given geometry and flow regime, the error function in Eq. (8) in conjunction with the cost map in Figure 6(a) determines whether WMLES is a viable approach in terms of accuracy of the quantity of interest and computational resources available. For the case of NASA Juncture Flow considered here, the geometry,  $Re$ , and  $Ma$  are set parameters. If we further assume that the error of a quantity  $\langle \mathbf{q} \rangle$  follows a power law (i.e., functional invariance under grid-size rescaling), Eq. (8) can be simplified as

$$\varepsilon_q = \beta_q \left( \frac{\Delta}{\delta} \right)^{\alpha_q}, \quad (9)$$

where  $\beta_q$  and  $\alpha_q$  are the error constant of proportionality and error convergence rate, respectively, that depend on the modeling approach (SGS model, wall model, numerical scheme,...) and flow regime (i.e., laminar flow, fully turbulent flow, separated flow,...).

We focus on the error scaling of the surface pressure coefficient ( $\varepsilon_p$ ) and mean velocity profile in outer units ( $\varepsilon_u$ ). It is certain that, from an engineering viewpoint, the lift and drag coefficients are the most pressing quantities of interest in aerodynamic applications. However, both are integrated quantities susceptible to error cancellation. They also lack information about the spatial structure of the flow, which makes more challenging the detection of modeling errors. On the other hand, the granularity provided by pointwise time-averaged quantities, such as the mean pressure and velocity, greatly facilitates the identification of modeling deficiencies. Hence, we will exploit the errors in pressure coefficient and mean velocity profile as a proxy to measure the quality of the WMLES solution.

## B. Reference error scaling for mean velocity profile and pressure coefficient

To aid the interpretation of the results, it is informative to derive theoretical estimations for the error scaling of the pressure coefficient, the mean velocity profile, and the wall stress in simplified flow scenarios. For wall-attached flows, errors in  $C_p$  can be assumed to be dominated by inviscid effects. Under the thin boundary-layer approximation, the wall-normal-integrated spanwise mean momentum equation yields  $\bar{p} + \overline{\rho v^2} \approx p_I \Rightarrow p_{\text{wall}} = p_I$ , where  $p_I$  is the inviscid farfield pressure and  $\overline{(\cdot)}$  is the average in the spanwise direction and time. Thus, the pressure at the surface is mostly controlled by the inviscid imprint of the outer flow and we can expect

$$\varepsilon_p = \beta_p \left( \frac{\Delta}{\delta} \right)^{\alpha_p} Re^0, \text{ with } \beta_p \ll 1, \alpha_p \approx 0. \quad (10)$$

Equation (10) implies that errors in  $C_p$  should be small even when the boundary layer is marginally resolved (i.e.,  $\Delta \approx \delta$ ), and should exhibit a weak dependence on the grid resolution.

The error scaling of the mean velocity profile can be estimated by assuming WMLES of a turbulent channel flow in

which the kinetic energy spectrum follows  $E_k \sim 1/\Delta^a$  and the velocity gradients scale as  $\partial u_i/\partial x_j \sim \sqrt{E_k}/\Delta$  [61]. The exponent  $a$  depends on the regime the SGS models operates in:  $a = -1$  for the shear-dominated range [62, 63] and  $a = -5/3$  for the inertial range [64]. Taking into account the scaling above, the expected error of the mean velocity profile is

$$\varepsilon_u = \beta_u \left( \frac{\Delta}{\delta} \right)^{\alpha_u} Re^0, \text{ with } \alpha_u = 0 \text{ or } \alpha_u = 1, \quad (11)$$

where  $\alpha_u = 0$  for  $\Delta/\delta$  lying on the shear-dominated region, and  $\alpha_u = 1$  for  $\Delta/\delta$  within the inertial range [61]. The constant  $\beta_u$  depends on the SGS model, numerical schemes, and error propagation from the upstream flow. In the case of turbulent channel flow (no upstream error propagation)  $\beta_u$  is bounded by the error of the inviscid solution such that  $\beta_u < O(10^{-1})$  as discussed below. The results from Eq. (11) also indicate that no improvement in the error is expected for grid resolutions comparable to the scales in the shear-dominated region, whereas an approximately linear scaling can be anticipated for finer grids with sizes comparable to the scales in the inertial range. The conclusion is consistent with the phenomenological argument that capturing the energy injection mechanism from the mean shear is critical to achieve accurate LES results.

The error scaling from Eq. (11) is validated for WMLES of turbulent channel flows at  $Re_\tau = 4200$ . The channels are driven by setting the center line velocity ( $U_c$ ) to a constant value akin to  $U_\infty$  in a turbulent boundary layer. The calculations are conducted with charLES using dynamic Smagorinsky model and the equilibrium wall model. We consider isotropic Voronoi grids with characteristic sizes of  $\Delta/\delta = 1/3, 1/5$ , and  $1/10$ , which are representative of the grid resolutions currently affordable for WMLES of the NASA Juncture Flow Experiment. Figure 7(a) shows the mean velocity profiles for the three grid resolutions and offers a visual reference of the convergence of the mean velocity to the DNS solution from Lozano-Durán and Jiménez [65]. The theoretical error scaling from Eq. (11) is tested in Figure 7(b). The figure also compares the errors from charLES (squares) with those obtained using a different numerical scheme and grid strategy, namely, finite differences with staggered grids (triangles) from Lozano-Durán and Bae [61] (see appendix B). The results show that  $\varepsilon_u \sim (\Delta/\delta)$  stands as a sensible approximation of the error for the two solvers considered, providing confidence in the theoretical arguments involved in the derivation of Eq. (11). A useful approximation of the error in charLES is  $\varepsilon_u \approx 0.08(\Delta/\delta)$ , which will be used later for comparison purposes with the NASA Juncture Flow. As a reference, Figure 7(b) also includes the largest error expected in a turbulent channel flow (dotted line) defined as the difference between the mean velocity from DNS and the inviscid solution, which gives an error of about  $\sim 15\%$ . Thus, even a low performance WMLES is bounded by a maximum error of  $\sim 15\%$  in canonical ZPGTBL (and channel flows) due to the constraint imposed by the freestream. Note that the reference inviscid error might be larger in more complex geometries.

Although not shown in Figure 7(b), the linear convergence predicted from Eq. (11) breaks down for  $\Delta \approx 0.03\text{--}0.05\delta$  due to the interplay between the numerical errors and the SGS model [61]. This anomaly does not manifest in our

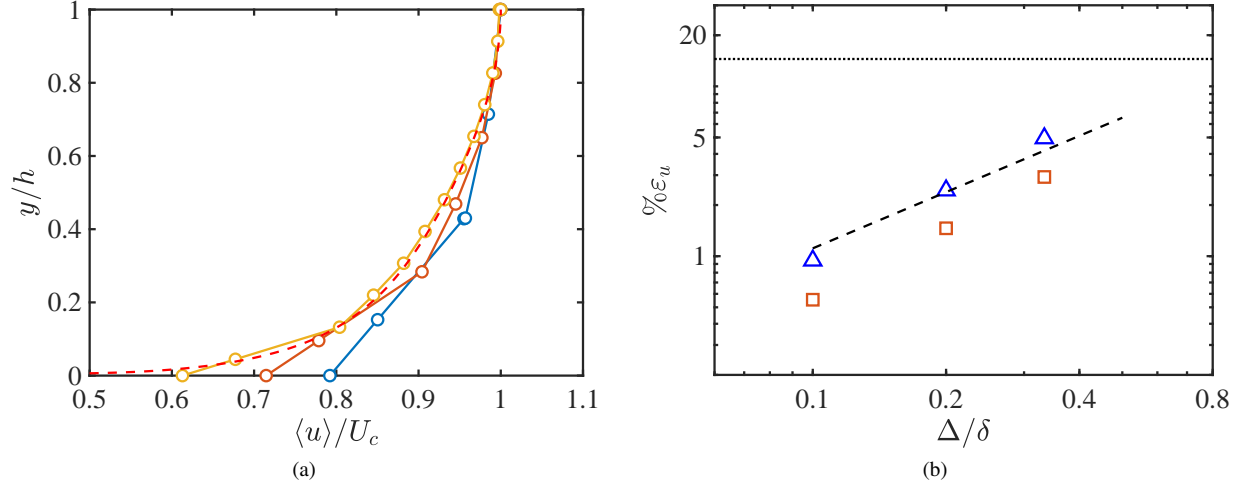


**Fig. 7** (a) The mean velocity profile for WMLES with charLES of a turbulent channel flow. The colors denote different grid resolutions  $\Delta/\delta = 1/3, 1/5$ , and  $1/10$ . (b) Error in the mean velocity profile  $\varepsilon_u$  as a function of the grid resolution  $\Delta$  for WMLES of turbulent channel flow. The symbols denote simulations using charLES with Voronoi grids ( $\square$ ) and finite-difference solver with staggered grids ( $\triangle$ ). The dashed line is  $\varepsilon_u \sim \Delta/\delta$ . The horizontal dotted line is the error from the inviscid solution.

NASA Juncture Flow calculations because of the choice of grid resolutions and will not be discussed here except for the comments in appendix B. Nonetheless, this behavior is responsible for the non-monotonic convergence of  $\varepsilon_u$  with  $\Delta$ , which is an outstanding problem of WMLES. Both charLES and the finite-difference solver suffer from this non-monotonic behavior, and the reader is referred to appendix B for more details.

The last important consideration is that Eq. (11) is meant to be valid for wall turbulence over approximately flat surfaces. In the case of flows in the vicinity of corners, corrections are required to account for the errors due to the proximity of lateral walls. Lozano-Durán and Bae [61] introduced a generalized version of Eq. (11) and showed that WMLES errors in the mean velocity profile at a given wall-normal distance ( $d$ ) are roughly controlled by the local shear length-scale,  $\varepsilon_u \sim \Delta/L_s$ , where  $L_s \approx u_\tau/S$  and  $S$  is the mean shear at  $d$ . Under the assumption that  $S \sim u_\tau/d$  (akin to the log layer), the error follows  $\varepsilon_u \sim \Delta/d$ . If we further assume that the error close to a corner is dominated by the influence of the closest wall (located at a distance  $d_{\min}$ ), we can define the compensated error as  $\varepsilon_u d_{\min}/\delta$ . The latter error will be instrumental to assessing the accuracy of WMLES in corner regions with respect to the reference error in turbulent channel flows.

### C. Wall-modeling errors

We analyze the error propagation between the mean velocity profile and the wall-stress predictions by the equilibrium wall model in Eq. (1). To that end, we express the quantity  $q$  in terms of its exact value  $\check{q}$  and its relative error  $\varepsilon_q$  as  $q = \check{q}(1 + \varepsilon_q)$ . Assuming that the matching location between LES and the wall model ( $h_w$ ) lies in the log layer, the



error in the LES wall-parallel velocity ( $u_{||}$ ) at the matching location is given by

$$\varepsilon_{u_{||}} = \frac{1 + \varepsilon_{u_\tau}}{1 + \varepsilon_\kappa} \left( 1 + \frac{\ln(1 + \varepsilon_{u_\tau}) + \check{\kappa}\check{B}(\varepsilon_\kappa + \varepsilon_B + \varepsilon_\kappa\varepsilon_B)}{\check{\kappa}\check{\phi}} \right) - 1, \quad (12)$$

where  $\check{\phi} = 1/\check{\kappa} \ln(Re_{h_w}) + \check{B}$  is the model reference solution,  $Re_{h_w} = \check{u}_\tau h_w / \nu$  is the Reynolds number based on the matching location, and  $\varepsilon_\kappa$  and  $\varepsilon_B$  are the relative errors in the model constants  $\kappa$  and  $B$ , respectively. Two sources of errors can be identified in Eq. (12): errors from the LES mean velocity ( $\varepsilon_{u_{||}}$ ) referred to as *external wall-modeling errors*, and errors from the model parameters ( $\varepsilon_\kappa$  and  $\varepsilon_B$ ), referred to as *internal wall-modeling errors*. In the former, errors in the LES mean velocity profile at the matching location propagate to the value of  $u_\tau$  predicted by the wall model. It can be shown that this error is roughly linear,  $\varepsilon_{u_\tau} \propto \varepsilon_{u_{||}}$ . This is seen in figure 8(a), which features the error in  $u_{||}$  as a function of the error in  $u_\tau$  evaluated from Eq. (12) for different values of  $\varepsilon_\kappa$  and  $\varepsilon_B$ . Figure 8(a) also includes the actual errors (circles) for WMLES of a turbulent channel flow using charLES with  $\Delta/\delta = 1/3, 1/5$ , and  $1/10$ , which follows the linear trend anticipated from our analysis. Note that this error can be labeled as external to the wall model inasmuch as it is present even if the wall model provides an exact representation of the near-wall region (i.e.,  $\varepsilon_\kappa = \varepsilon_B = 0$ ). Although not shown, the sensitivity of  $\varepsilon_{u_\tau}$  to  $Re_{h_w}$  is weak and scales as  $\varepsilon_{u_{||}} \sim \ln(Re_{h_w})$ .

The second source of errors represents the internal wall-model limitations: even with a perfect prediction of  $u_{||}$  (namely,  $\varepsilon_{u_{||}} = 0$ ), the wall model might incur errors due to i) uncertainties in the parameters  $\kappa$  and  $B$  embedded into the model, ii) deviations of the actual flow from these parameters (e.g., pressure gradient effects or roughness changing  $\kappa$  and  $B$ ), and/or iii) the fact that the log-layer law is no longer representative of the mean velocity profile (e.g., as in separated flows). A consequence of internal errors is that WMLES might not converge to the DNS solution with grid refinements until  $\Delta$  is in the DNS-like regime and the contribution of the wall model is negligible. Figure 8(b) quantifies the internal errors in the mean velocity profile as a function of  $\varepsilon_\kappa$  (solid lines) and  $\varepsilon_B$  (dashed lines). Overall, wall models are more resilient to internal errors than to external errors. For example, purely internal errors of  $\varepsilon_\kappa = 10\%$  and  $\varepsilon_B = 10\%$  yield  $\varepsilon_{u_\tau} \approx 6\%$  and  $\varepsilon_{u_\tau} \approx 3\%$ , respectively, both of them lower than the sole external error  $\varepsilon_{u_\tau} \approx \varepsilon_{u_{||}} = 10\%$ . Another interesting observation from Figure 8(a) is that certain combinations of  $\varepsilon_\kappa$ ,  $\varepsilon_B$  and  $\varepsilon_{u_{||}}$  are subject to error cancellation, resulting in a fortuitous good prediction of  $u_\tau$ . Note that the expression in Eq. (12) might be used even when the near-wall flow does not comply with the log-layer law; however in that case  $\varepsilon_\kappa$  and  $\varepsilon_B$  become arbitrarily large and Eq. (12) ceases to be informative of the error scaling.

In summary, external errors will propagate linearly to the mean velocity profile, increasing  $\beta_u$  without affecting  $\alpha_u$  appreciably, while internal errors will bound the maximum possible accuracy of the WMLES solution. Both sources of error, external and internal, will impact the predictions of the NASA Juncture Flow.

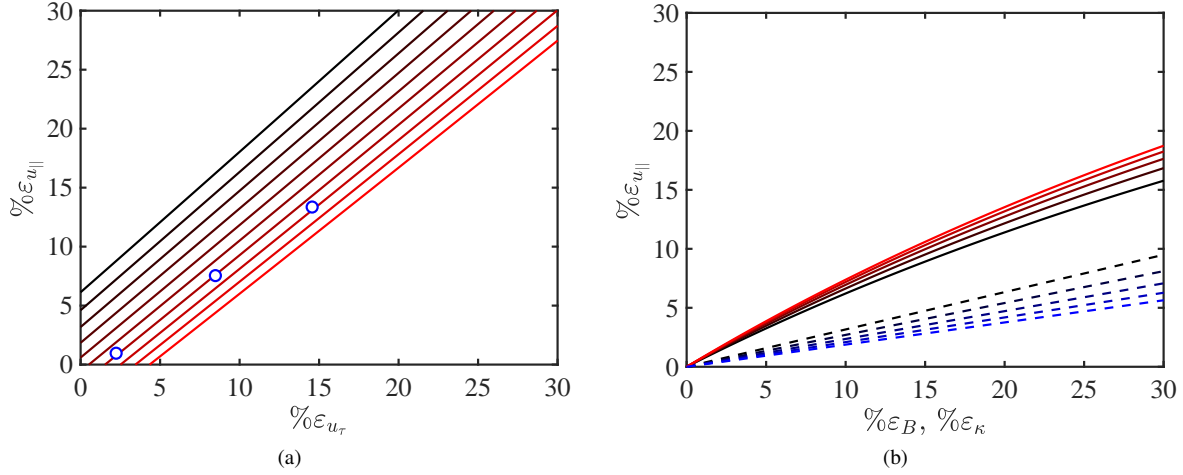


**Fig. 8** Error propagation between LES and wall model from Eq. (12). (a) Error in the LES wall-parallel velocity  $u_{||}$  at the matching location as a function of the error in the wall-stress predicted by the equilibrium wall. The solid lines represent  $\varepsilon_{\kappa} = \varepsilon_B = -10\%, -7.5\%, -3.5\%, -1\%, 1\%, 3.5\%, 7.5\%, 10\%$  from black to red and  $Re_{h_w} = 1000$ . The circles are the actual errors measured by WMLES of turbulent channel flows with charLES for  $\Delta/\delta = 1/3, 1/6$  and  $1/10$ . (b) Error in the LES wall-parallel velocity  $u_{||}$  at the matching location as a function of the error in the model parameters  $\kappa$  (solid lines) and  $B$  (dashed lines) for different values of matching location Reynolds number  $Re_{h_w} = 100, 300, 1000, 3000$ , and  $10000$  from black to red/blue.

## V. WMLES of the NASA Juncture Flow Experiment

### A. WMLES Cases and uncertainties

We perform WMLES of the NASA Juncture Flow with a leading-edge horn at  $Re = 2.4 \times 10^6$  and  $AoA = 5^\circ$ . Eight cases are considered. In the first six cases, we employ grids generated using strategy (i) with constant grid-size in millimeters similar to the example offered in Figure 4(a). In this case, the direct impact of  $Re_{\Delta}^{\min}$  can be absorbed into  $\Delta/\delta$  as argued for Eq. (9). The grid sizes considered are  $\Delta \approx 6.7, 4.3, 2.2, 1.1$ , and  $0.5$  mm, which are labeled as C-D7, C-D4, C-D2, C-D1, and C-D0.5, respectively. Cases C-D7, C-D4, and C-D2 are obtained by refining the grid across the entire aircraft surface. For cases C-D1 and C-D0.5, the grid size is  $1.1$  and  $0.5$  mm, respectively, only within a box along the fuselage and wing-body juncture defined by  $x \in [1770, 2970]$  mm,  $y \in [-300, -200]$  mm, and  $z \in [-50, 150]$  mm. The purpose of C-D1 and C-D0.5 is to further examine the convergence of the solution in the separated region, where we will show the performance of WMLES is the poorest. The refinement box was chosen to make the cases computationally tractable. The computational cost  $N_c$  of the simulations was  $31 \times 10^3, 40 \times 10^3, 75 \times 10^3, 116 \times 10^3, 398 \times 10^3$  core-hours for C-D7, C-D4, C-D2, C-D1, and C-D0.5, respectively, using Intel(R) Xeon(R) CPU E5-2670 0 @ 2.60GHz (in the NASA Advanced Supercomputing facility Pleiades). The total number of control volumes is 14, 17, 31, 50 and 174 million for C-D7, C-D4, C-D2, C-D1, and C-D0.5, respectively. Nonetheless, one should be cautious in appraising the number of control volumes as an indicator of the accuracy of the solution as discussed in Section V.C). A more sensible characterization of the grid resolution is given by the *resolution map*:

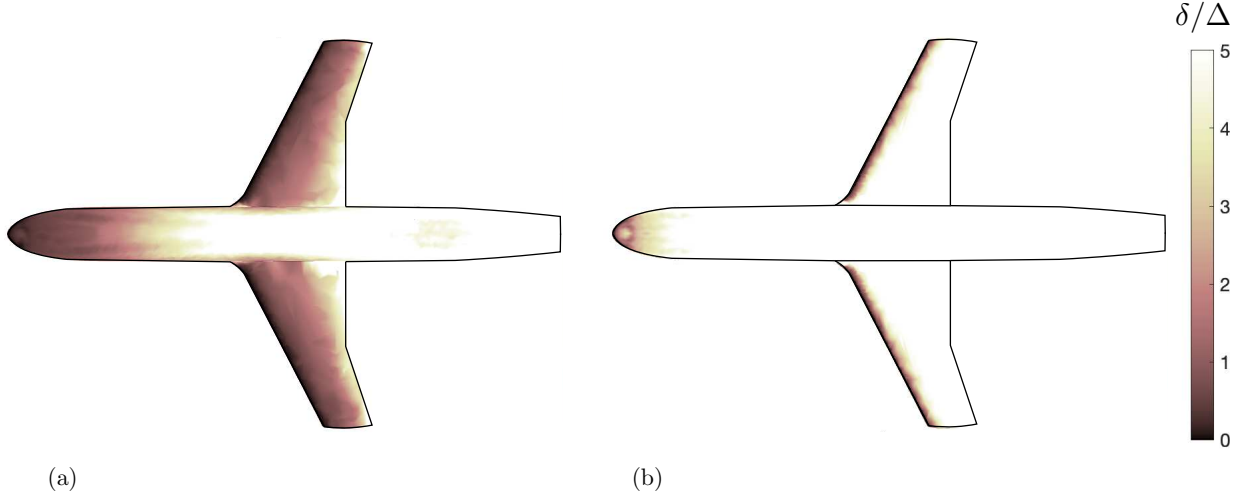


**Fig. 9 Resolution map: points per boundary layer thickness ( $\delta/\Delta$ ) for (a) constant-size grid for case C-D2 and (b) BL-conforming grid for case C-N5-R2e3. The colormap is clipped at  $\delta/\Delta = 5$  to facilitate the comparison between panel (a) and (b), but note that white areas might enclose regions with  $\delta/\Delta > 5$ .**

distribution of points per boundary layer thickness ( $\delta/\Delta$ ) over the aircraft surface. Figure 9(a) features the resolution map for case C-D4 and exposes the strong inhomogeneity in  $\delta/\Delta$  typical of constant-size grids.

Three additional cases are considered to assess the impact of BL-conforming grids on the accuracy of the predictions. The grids are generated using strategy (ii) for  $N_{bl} = \delta/\Delta = 5$  and  $Re_{\Delta}^{\min} = 2.8 \times 10^3$  (denoted as case C-N5-R2e3);  $N_{bl} = \delta/\Delta = 10$  and  $Re_{\Delta}^{\min} = 2.8 \times 10^3$  (C-N10-R2e3); and  $N_{bl} = \delta/\Delta = 5$  and  $Re_{\Delta}^{\min} = 5.6 \times 10^3$  (C-N5-R5e3). The first two cases are intended to provide information about the effect of  $N_{bl}$  on the accuracy of the results, whereas the third case is used to evaluate the impact of the leading-edge resolution. The grid Reynolds numbers considered set the minimum allowed grid resolution to  $\Delta_{\min} \approx 0.6$  mm,  $\Delta_{\min} \approx 0.3$  mm, and  $\Delta_{\min} \approx 1.3$  mm for cases C-N5-R2e3, C-N10-R2e3, and C-N5-R5e3, respectively. A cross section of the BL-conforming grid for C-N5-R2e3 is shown in Figure 4(b). The computational cost  $N_c$  of the simulations was  $27 \times 10^3$ ,  $90 \times 10^3$ , and  $13 \times 10^3$  core-hours for C-N5-R2e3, C-N10-R2e3, and C-N5-R5e3 respectively, using Intel(R) Xeon(R) CPU E5-2670 0 @ 2.60GHz. The total number of control volumes for C-N5-R2e3, C-N10-R2e3, and C-N5-R5e3 is 12, 40, and 6 million, respectively. Figure 9(b) shows the resolution map for C-N5-R2e3. Compared to the constant-size grid counterpart in Figure 9(a), BL-conforming grids display an homogeneous grid resolution in terms of  $\delta/\Delta$  except at the leading-edge region, where the limitation imposed by  $Re_{\Delta}^{\min}$  comes into effect. An instantaneous visualization of the Q-criterion [66] for case C-N5-R2e3 is shown in Figure 10 to provide a general overview of turbulent flow around the Juncture Flow geometry.

In the following,  $\langle q \rangle$  and  $(q)'$  denote the time-average and the fluctuating component of  $q$ , respectively. For comparison purposes, the profiles from WMLES are interpolated to the locations of the experiments. Statistical uncertainties owing to limited samples in WMLES quantities are estimated assuming uncorrelated and randomly



**Fig. 10 Visualization of the instantaneous isosurfaces of the Q-criterion colored by the velocity magnitude. Data for C-N10-R2e3.**

distributed errors following a normal distribution. The uncertainty in  $\langle q \rangle$  is then estimated as  $\langle q \rangle_u \equiv \sigma / \sqrt{N_s}$ , where  $N_s$  is the number of samples in  $\langle q \rangle$ , and  $\sigma$  is the standard deviation of the samples. The uncertainties were computed for all the quantities of interest, but are only reported for the tangential Reynolds stresses. The uncertainties for the mean velocity profiles and pressure coefficient were found to be below 1% and are not included in the plots.

### B. Mean velocity profiles with constant-size grids

Three locations are considered to investigate the errors in the mean velocity profile: (i) the upstream region of the fuselage ( $x = 1168.40$  mm,  $z = 0$  mm), (ii) the wing-body juncture ( $x = 2747.6$  mm,  $y = 239.1$  mm), and (iii) wing-body juncture with separation close to the trailing edge ( $x = 2922.6$  mm,  $y = 239.1$  mm). Figure 11 portrays the three locations in the NASA Juncture Flow using solid lines of different colors. Throughout the manuscript, we often refer to the three regions simply as fuselage, juncture and separation/trailing-edge regions. We will assume that the mean velocity from WMLES is directly comparable to unfiltered experimental data  $\langle u_i^{\text{exp}} \rangle$ , as it is case for quantities dominated by large-scale motions [61, 67]. The results for WMLES with constant-size grids are presented next.

The mean velocity profiles at the fuselage, juncture, and trailing-edge region are shown in panel (a) of Figure 12, 13, and 14, respectively. In the fuselage, the mean velocity profiles approach the experimental results with grid refinement. The turbulent boundary layer over the fuselage is about 10 to 20 mm thick, which yields roughly 3–6 points per boundary-layer thickness for the grid resolutions considered. The mean velocity profiles also get closer to the experimental profile in the juncture region and trailing-edge zone, as seen in Figures 13(a) and 14(a), but they do so at

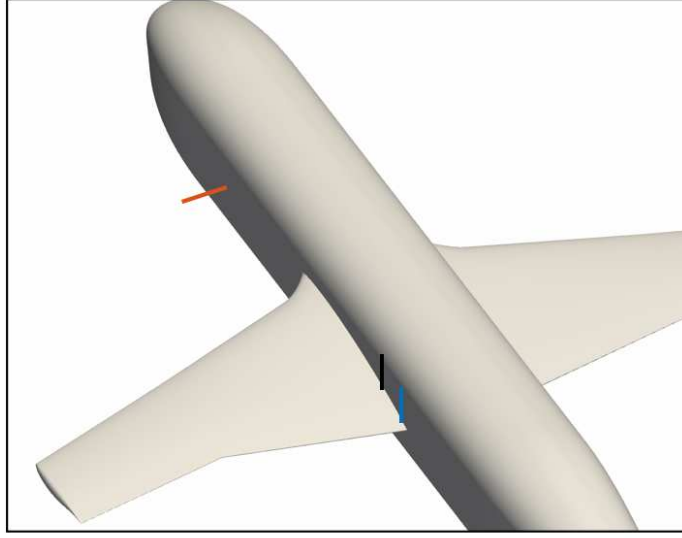
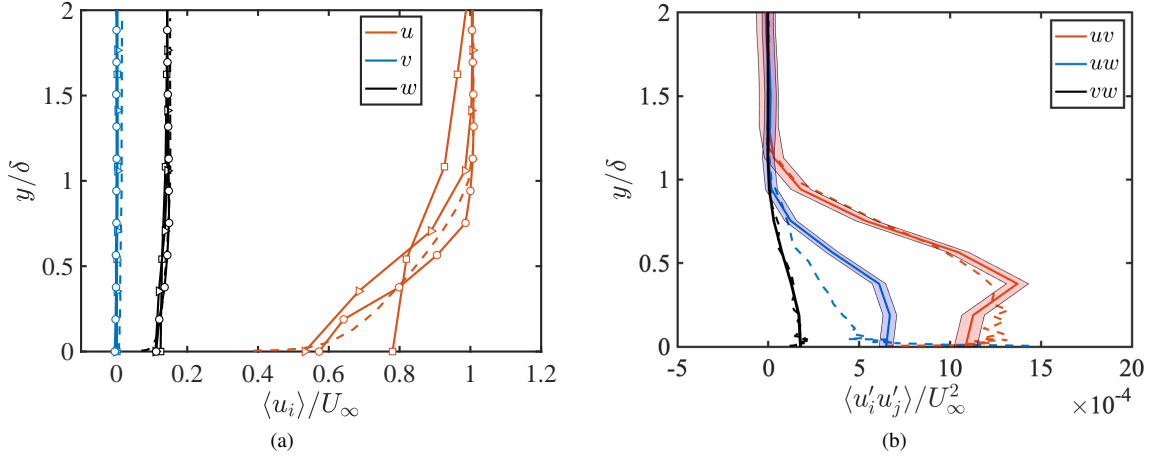


**Fig. 11** The three locations considered (solid lines) to investigate the error in the mean velocity profile: red (fuselage), black (junction), and blue (separation).

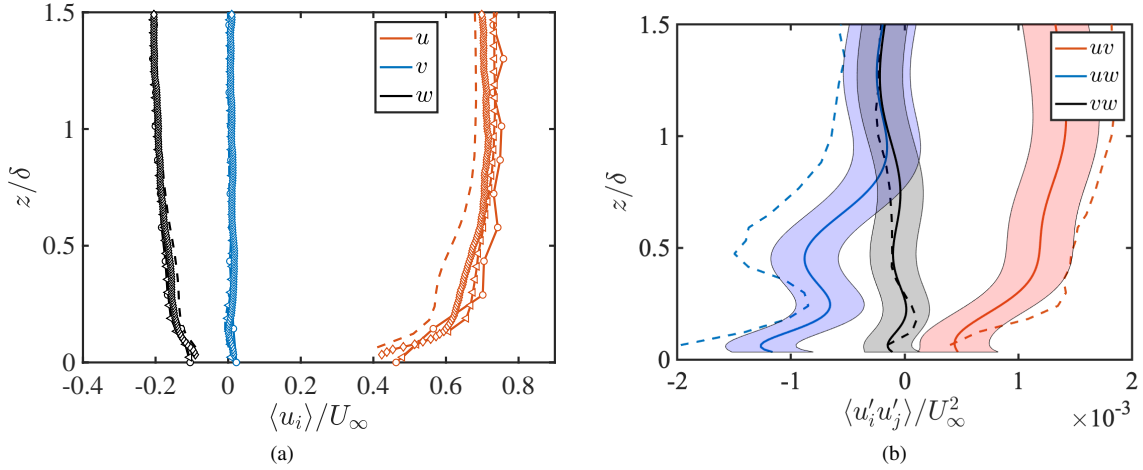
a slower pace. The accuracy of the predictions in the latter regions appears to be inferior than those in the fuselage despite the fact that the local  $N_{bl}$  in the junction and trailing-edge is roughly 30–80 points per  $\delta$ , which is one order of magnitude larger than  $N_{bl}$  in the fuselage.

Figure 15 is the cornerstone of the present study. It summarizes the relative errors in the prediction of the mean velocity profile as a function of the local grid resolution. Figure 15 also follows the same color code as Figure 11 and features the reference error for a turbulent channel flow (dotted line) introduced in Section IV. In the fuselage, the errors are roughly 3%–8% and scale as  $\varepsilon_u \approx \beta_u (\Delta/\delta)$  (red symbols in Figure 15(a)) akin to the errors in a turbulent channel flow. This suggest that the turbulent flow in the fuselage resembles a ZPGTBL. As such, wall- and SGS models devised for, and validated in, flat-plate turbulence perform as anticipated by the error analysis in Section IV. The error constant in the fuselage,  $\beta_u \approx 0.14$ , is larger than the value for turbulent channel flows,  $\beta_u \approx 0.08$  (see Section IV), and it will be shown in §V.C that this is caused by the propagation of errors from upstream of the fuselage.

In contrast, the wing-body junction and trailing-edge region exhibit larger errors than those reported in the fuselage. In the junction region, the errors in the mean velocity are about 15% (black symbols in Figure 15a), whereas the errors in the trailing-edge zone are about 100% (blue symbols in Figure 15a). One of the reasons for the larger errors in the junction and trailing-edge is that the mean profiles are plotted along a line parallel and close to the fuselage (see black and blue lines in Figure 11). As argued in Section IV, this would amplify the errors due to the additional shear from the fuselage boundary-layer. To account for enhanced errors in the proximity of a wall, Figure 15(b) shows the errors



**Fig. 12** (a) Mean velocity profiles and (b) Reynolds shear stresses at location 1: upstream region of the fuselage  $x = 1168.4$  mm and  $z = 0$  mm (red line in Figure 11). Solid lines with symbols denote WMLES for cases C-D7 ( $\square$ ), C-D4 ( $\triangleright$ ), and C-D2 ( $\circ$ ). Colors denote different velocity components. Panel (b) only includes case C-D2 and the shaded area represents statistical uncertainty. Experiments are denoted by dashed lines. The distance  $y$  is normalized by the local boundary-layer thickness  $\delta$  at that location.



**Fig. 13** (a) Mean velocity profiles and (b) Reynolds shear stresses at location 2: wing-body juncture at  $x = 2747.6$  mm and  $y = 239.1$  mm (black line in Figure 11). In panel (a), lines with symbols are for cases C-D2 ( $\circ$ ), C-D1 ( $\triangleleft$ ), and C-D0.5 ( $\diamond$ ). Colors denote different velocity components. Panel (b) only includes case C-D0.5 and the shaded area represents statistical uncertainty. Experiments are denoted by dashed lines. The distance  $z$  is normalized by the local boundary-layer thickness  $\delta$  at that location.

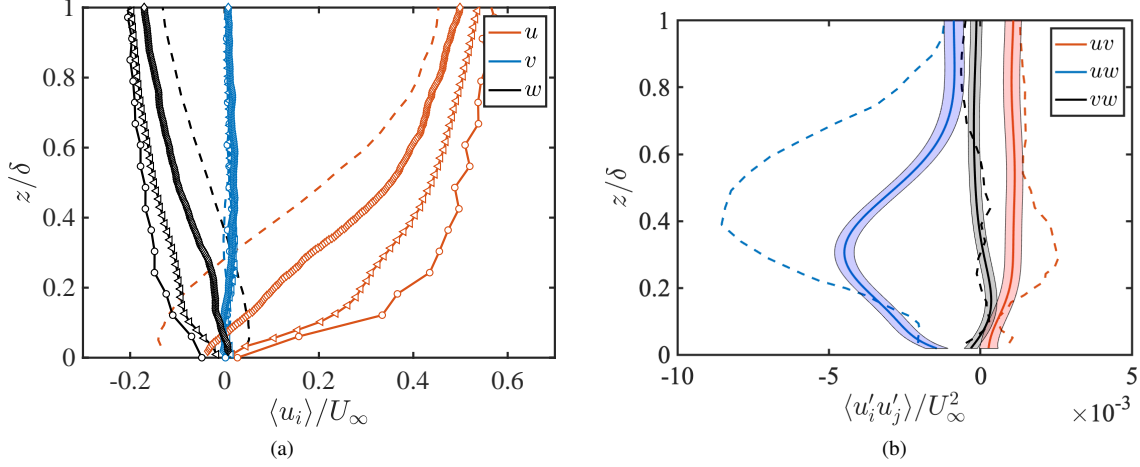


**Fig. 14** (a) Mean velocity profiles and (b) Reynolds shear stresses at location 3: wing-body juncture close to the trailing-edge at  $x = 2922.6$  mm and  $y = 239.1$  mm (blue line in Figure 11). In panel (a), lines with symbols are for cases C-D2 ( $\circ$ ), C-D1 ( $\triangleleft$ ), and C-D0.5 ( $\diamond$ ). Panel (b) only includes case C-D0.5 and the shaded area represents statistical uncertainty. Experiments are denoted by dashed lines. The distance  $z$  is normalized by the local boundary-layer thickness  $\delta$  at that location.

compensated by the closest distance to the fuselage  $d_{\min}/\delta$ . The compensated errors in the juncture region bear a closer resemblance to the trends observed in the fuselage, implying that most of the increase in error can be explained by the proximity of the wall. Nonetheless, the convergence rate of the solution at the juncture,  $\alpha_u \approx 0.4$ , is still slower than the linear convergence expected from the channel reference error from §IV.B. The situation is less favorable for the trailing-edge region: not only is the convergence rate slower ( $\alpha_u \approx 0.6$ ), but its magnitude is still considerably larger (i.e., higher  $\beta_u$ ) even after error compensation. This suggests that the errors in the separated region are not only the consequence of the proximity to the fuselage but of something else. The additional errors and slower convergence rate in the wing-body juncture and trailing-edge may be attributed to two causes. The first one might be the contamination of the solution from upstream errors. The second option is that the presence of three-dimensional boundary layers and/or flow separation renders inaccurate the modeling assumptions predicated upon the local similarity to a ZPGTBL [68]. The first source of error is examined in more detail in the following section using BL-conforming grids.

For completeness, we close this section by briefly discussing the errors in the prediction of the tangential Reynolds shear stresses. Panel (b) of Figures 12, 13 and 14 contains the resolved portion of the tangential Reynolds shear stresses,  $\langle u'_i u'_j \rangle$ . The profiles of  $\langle u'_i u'_j \rangle$  capture the trends of the experimental data at the stations investigated, although their magnitudes are underpredicted for the juncture region and trailing edge. Lozano-Durán and Bae [61] showed that the values of the SGS tensor ( $\tau_{ij}^{\text{SGS}}$ ) required to predict the correct mean velocity profile usually imply the underestimation of  $\langle u'_i u'_j \rangle$ . Assuming that  $\langle u_i^{\text{exp}} \rangle \approx \langle u_i \rangle$ , then  $\langle u_i^{\text{exp}} u_j^{\text{exp}} \rangle \approx \langle u'_i u'_j \rangle + \langle \tau_{ij}^{\text{SGS}} \rangle$ . Thus, for the typical grid sizes in WMLES, we expect that  $|\langle u'_i u'_j \rangle| < |\langle u_i^{\text{exp}} u_j^{\text{exp}} \rangle|$ , i.e., underprediction of the tangential Reynolds stress. Estimations from

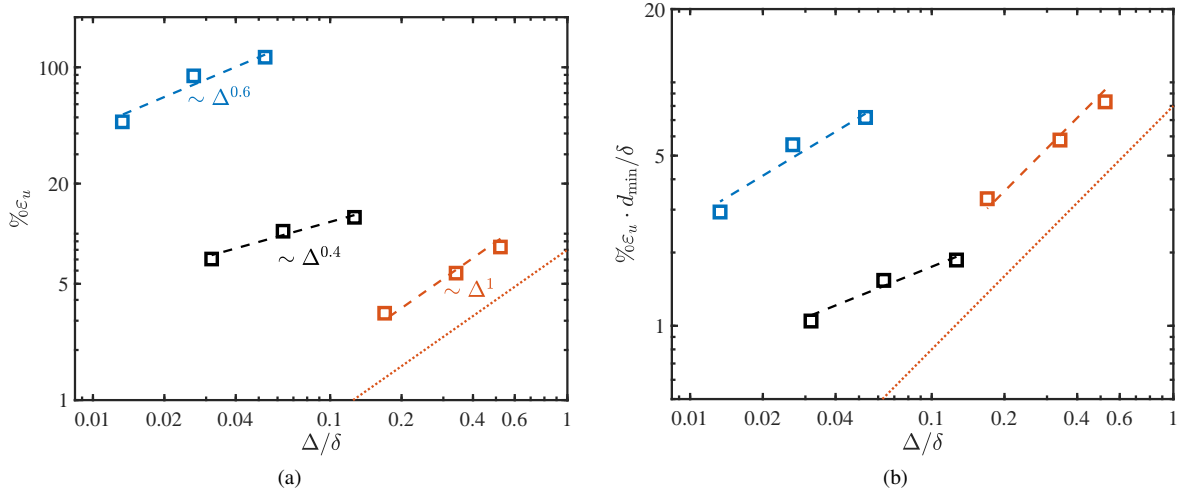


**Fig. 15** Errors in the mean velocity profile (symbols) at the three locations shown in Figure 11 using the same color code: red (fuselage), black (junction), and blue (separation). (a) Error in the mean velocity profile predicted by WMLES as a function of the grid resolution normalized with the local boundary-layer thickness. (b) Error in the mean velocity profile predicted by WMLES compensated by the closest distance to fuselage  $d_{\min}/\delta$  as a function of the grid resolution. We have set  $d_{\min} = \delta$  for the fuselage location. The red dotted line in panels is the reference error for a turbulent channel flow,  $\epsilon_u = 0.08\Delta/\delta$ .

Lozano-Durán and Bae [61] also showed that the error for the turbulence intensities in WMLES grids should scale as  $\sim (\Delta/\delta)^{2/3}$  with values in the range of 10–30%, which is consistent with our observations.

### C. Mean velocity profiles with BL-conforming grids

We evaluate the benefits of utilizing BL-conforming grids constructed following the procedure described in Section III.A. First, we illustrate the improvements in the prediction of the mean velocity by comparing the results for case C-D2 ( $\Delta \approx 2$  mm) with case C-N5-R2e3 ( $N_{bl} = 5$  and  $Re_{\Delta}^{\min} = 2.8 \times 10^3$ ). The mean velocity profiles for both cases are shown in Figure 16 at the three locations under consideration. Moderate improvements are attained for C-N5-R2e3 at the fuselage, despite the fact C-N5-R2e3 and C-D2 share the same  $N_{bl}$  at that location. The benefits enabled by BL-conforming grids are accentuated at the junction region and trailing edge, at which C-N5-R2e3 outperforms C-D2 using only one fourth of the number of grid points in each spatial direction (namely, a factor of 64 less points in the local volume). For reference, case C-D2 has 31 million control volumes, whereas case C-N5-R2e3 has 12 million control volumes. The lower errors for case C-N5-R2e3 clearly demonstrate that the sole use of the number of control volumes is a misleading metric to quantify the quality of WMLES, and that the spatial distribution of control volumes may have an appreciable impact on the accuracy of the solution.

The systematic characterization of errors in the mean flow is shown in Figure 17(a), which includes the errors for constant-size grid (open symbols) and BL-conforming grids (closed symbols). The predictions obtained with



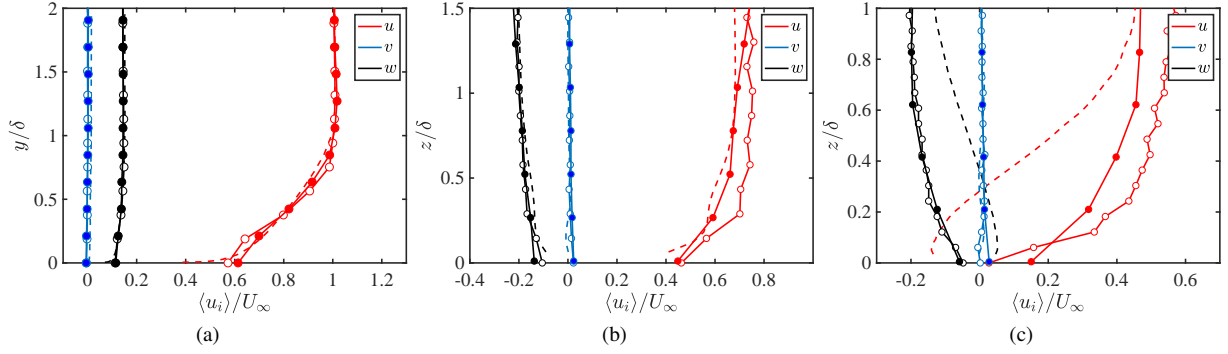


**Fig. 16** Mean velocity profiles for case C-N5-R2e3 (solid lines with •) and C-D2 (solid lines with ◊) at (a) location 1: upstream region of the fuselage  $x = 1168.4$  mm and  $z = 0$  mm (b) location 2 wing-body juncture  $x = 2747.6$  mm and  $y = 239.1$  mm, and (c) location 3: wing-body juncture close to the trailing edge at  $x = 2922.6$  mm and  $y = 239.1$  mm. Experiments are denoted by dashed lines. Colors denote different velocity components. The distance  $y$  is normalized by the local boundary-layer thickness  $\delta$  at that location. (d) Error in the mean velocity profile prediction by WMLES as a function of the grid resolution. Open symbols represent constant-size grids (same as in figure 15a) and closed symbols represent BL-conforming grids. The different colors denote the three locations as in Figure 15(b) using the same color code.

BL-conforming grid are consistently more accurate than those for constant-size grid at the three locations considered. The improvements in the fuselage region are the least pronounced, which might be an indication that the errors saturate roughly at 2%. This is consistent with the error analysis in Section IV, where it was demonstrated that internal wall-modeling errors caused by deviations of the actual flow from the law-of-the-wall propagate to the mean velocity profile as dictated by Eq. (12). These internal errors impose a lower limit to the minimum error achievable by WMLES. For example, if the flow at the fuselage differs from a ZPGTBL by 3% ( $\% \varepsilon_\kappa = 3$ ), the minimum error attainable by WMLES at that location would be 2%, which is consistent with our observations. Moreover, additional grid refinements in the presence of internal errors are not expected to improve the prediction of the mean velocity profile until the LES grid resolution (and  $h_w$ ) reaches the wall-resolved-LES regime, for which internal errors would vanish. For the juncture and separation region, the most noticeable improvement with BL-conforming grids is the reduction in the error constant  $\beta_u$ , while the convergence rate of the error  $\alpha_u$  remains unchanged. Thus, grids designed to specifically target the boundary layer can improve the overall accuracy of WMLES via a smaller value of  $\beta_u$ .

The improved outcome for BL-conforming grids might be justified by considering the upstream history of the WMLES solution at a given station. For the sake of simplicity, let us consider WMLES of a flat-plate turbulent boundary layer evolving along the  $x$  direction using two grids as those shown in Figure 3: a constant-size grid and a BL-conforming grid. Given an  $x$ -location at which both grids share the same  $N_{bl}$ , the upstream flow for the constant-size grid is underresolved compared to the BL-conforming grid due to the thinning of  $\delta$ . Consequently, constant-size grids display larger upstream errors that eventually propagate downstream, contaminating the solution at  $x$ . Even if at a given  $x$ -location  $N_{bl}$  is larger for the constant-size grid than for the BL-conforming grid, the solution for the former

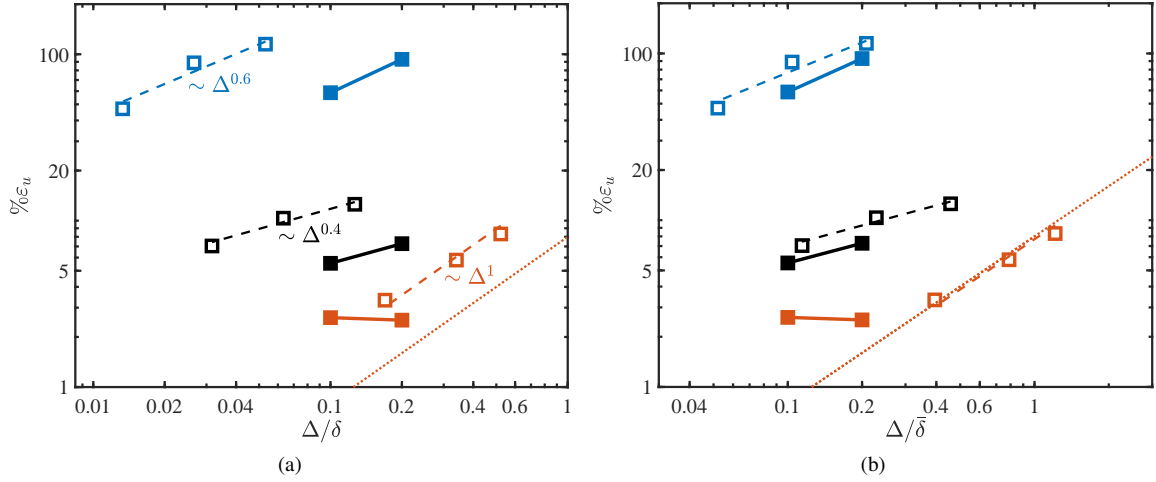


**Fig. 17** Errors in the mean velocity profile (symbols) at the three locations shown in Figure 11 using the same color code: red (fuselage), black (juncture), and blue (separation). (a) Error in the mean velocity profile predicted by WMLES as a function of the grid resolution normalized with the local boundary-layer thickness. (b) Error in the mean velocity profile predicted by WMLES as a function of the effective upstream-averaged grid resolution  $\Delta/\bar{\delta}$ . The value of  $\bar{\delta}$  was calculated for  $\Delta x_e = 300\delta_0$ . Open symbols denote constant-size grids and closed symbols denote BL-conforming grids. The red dotted line in panels is the reference error for a turbulent channel flow,  $\epsilon_u = 0.08\Delta/\delta$ .

could still exhibit poor accuracy because of the propagation of upstream errors. Assuming that the lifetimes of the energy-containing eddies at  $x_0 < x$  are proportional to  $\delta_0/u_\tau$ , and that these eddies are advected by  $U_\infty$ , the spatial extent for the downstream propagation of errors,  $\Delta x_e$ , from a given location  $x_0$  can be estimated as  $\Delta x_e \approx \Gamma U_\infty \delta_0 / u_\tau$ , where  $\Gamma$  is a flow-dependent constant. The distance  $\Delta x_e$  is the streamwise recovery length for the energy-containing eddies to forget their past history, and hence their errors. In ZPGTBL at high  $Re$ ,  $\Delta x_e$  has been experimentally shown to reach values of  $\Delta x_e \approx 300\delta_0$  [69]. In our case, this implies that errors from the underresolved leading edge ( $\delta_0 \approx 1$  mm) are advected downstream for  $\Delta x_e \approx 300$  mm, which is  $\sim 50\%$  of the crank chord. On the other hand, the BL-conforming grids maintain a constant grid resolution scaled in  $\delta$  units and effectively a higher resolution of the upstream flow.

One implication of the downstream propagation of errors is that the local grid resolution  $\Delta/\delta$  is inappropriate to characterize the errors in constant-size grids. Instead, an effective upstream-averaged grid resolution of the form  $\Delta/\bar{\delta}$  should be used, where  $\bar{\delta}(x, y, z) = \int_{-\infty}^x G(x' - x) \delta(x', y, z) dx$  with  $G$  the Gaussian kernel  $G(x) = 1/(\sqrt{2\pi}\Delta x_e) \exp[-1/2x^2/(2\Delta x_e)^2]$  or any other similar kernel. The new effective grid resolution is tested in Figure 17(b), which shows the errors in the mean velocity as a function of  $\Delta/\bar{\delta}$ . In the fuselage, the errors for constant-size grids collapse with the reference error from turbulent channel flows, confirming that the diminished performance of constant-size grids is merely a matter of downstream error propagation. The collapse of the errors at the juncture and trailing-edge regions is also significantly improved between constant-size and BL-conforming grids using  $\Delta/\bar{\delta}$ , suggesting that the same argument applies to these cases as well. Errors in the fuselage for BL-conforming grids

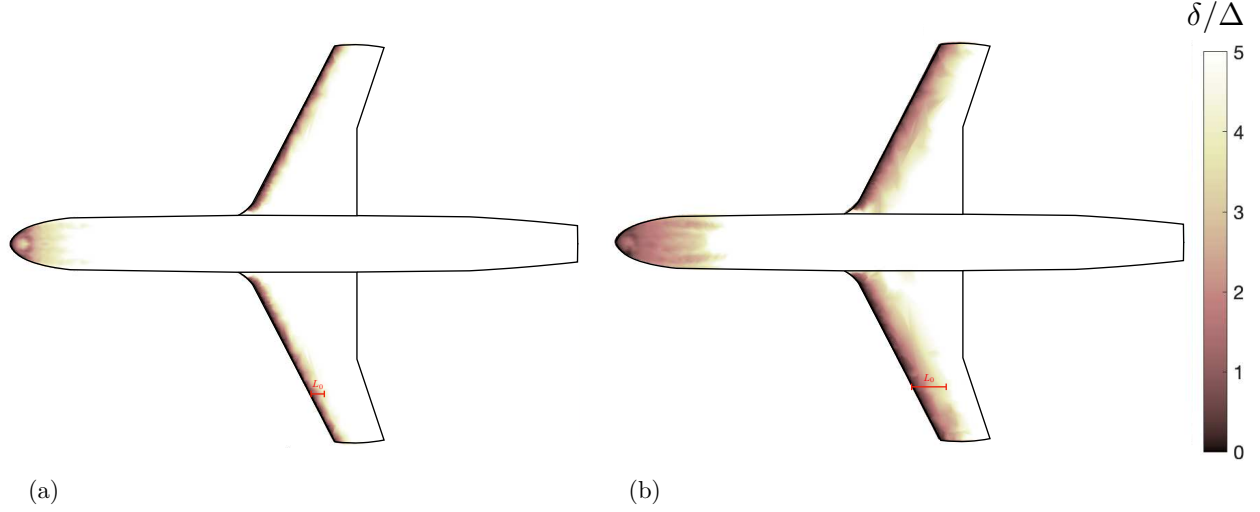


**Fig. 18** Resolution map to test the effect of leading-edge grid solution. Points per boundary layer thickness ( $\delta/\Delta$ ) for (a) case C-N5-R2e3 ( $Re_{\Delta}^{\min} = 2.8 \times 10^3$ ) and (b) case C-N5-R5e3 ( $Re_{\Delta}^{\min} = 5.6 \times 10^3$ ).  $L_0$  denotes the streamwise extent of the underresolved leading-edge, i.e., region with  $\delta/\Delta < N_{bl}$ .

remain saturated at roughly 2%. In general, constant-size grids display a lower effective resolution ( $\Delta/\delta < \Delta/\bar{\delta}$ ) than BL-conforming grids ( $\Delta/\delta \approx \Delta/\bar{\delta}$  for  $Re_{\Delta}^{\min} < Re_x$ ), which explains the poorer performance of the former. Hence, the long convective distance for error propagation from the leading edge combined with the higher upstream errors for constant-size grids accounts for the improved performance of BL-conforming grids reported in Figure 17(a).

#### D. Effect of leading-edge grid resolution

The effect of leading-edge resolution on the accuracy of the mean velocity profiles is evaluated by comparing C-N5-R2e3 and C-N5-R5e3. Both cases share the same points per boundary-layer thickness ( $\delta/\Delta = 5$ ) but differ on the value of  $Re_{\Delta}^{\min}$ , namely  $Re_{\Delta}^{\min} = 2.6 \times 10^3$  and  $Re_{\Delta}^{\min} = 5.8 \times 10^3$  for C-N5-R2e3 and C-N5-R5e3, respectively. It was argued that  $Re_{\Delta}^{\min}$  can be understood as a quantification of the leading-edge grid resolution such that, for constant  $N_{bl}$ , decreasing  $Re_{\Delta}^{\min}$  implies finer resolution at the leading-edge. Other characterizations of the leading-edge resolution instead of  $Re_{\Delta}^{\min}$  are possible and an alternative is discussed in Appendix A. A comparison of the resolution maps for cases C-N5-R2e3 and C-N5-R5e3 is presented in Figure 18. Increasing the value of  $Re_{\Delta}^{\min}$  by a factor of two lessens the portion of the wing area resolved with  $N_{bl} = 5$ . Following the assumptions introduced in §III.B for ZPGTBL, the streamwise extent of the underresolved leading-edge region ( $L_0$ , see Figure 3b) scales as  $L_0/L \sim (Re_{\Delta}^{\min} N_{bl})^{7/6} Re^{-1}$  in first order approximation. Thus, increasing  $Re_{\Delta}^{\min}$  by a factor of two will roughly double  $L_0$ , consistent with the growth of the shading area observed in Figure 18.

The consequences of diminished leading-edge grid resolution are appraised in Figure 19(a,b,c), which compares the mean velocity profiles for C-N5-R2e3 and C-N5-R5e3 at the three locations considered. Unsurprisingly, the mean

velocity profiles improve for decreasing  $Re_{\Delta}^{\min}$ . The relative error in the mean velocity profile as a function of  $Re_{\Delta}^{\min}$  is shown in Figure 19(d), which quantifies more rigorously the dependence of  $\varepsilon_u$  with  $Re_{\Delta}^{\min}$ . A simple model for the propagation of errors from the underresolved leading-edge to the downstream location  $x$  can be constructed by assuming that  $\varepsilon_u$  will decay linearly with the streamwise distance to the leading-edge,  $\varepsilon_u \sim 1/N_{bl}(1 + \Gamma\delta_{\min}/\Delta L)$ , where  $\delta_{\min}$  is the minimum  $\delta$  resolved with  $N_{bl}$  points,  $\Delta L = x - L_0$  is the distance to the underresolved leading-edge, and  $\Gamma$  controls the lasting effects of errors propagation (as discussed in the previous section). For  $\Delta L \rightarrow \infty$  (i.e.,  $x$  far from the leading-edge), the model recovers  $\varepsilon_u \sim 1/N_{bl} = \Delta/\delta$  (i.e., no influence from leading-edge errors). Expressing the errors in terms of the grid parameters ( $N_{bl}, Re_{\Delta}^{\min}$ ) under the assumption of ZPGTBL yields  $\varepsilon_u \sim 1/N_{bl}[1 + \Gamma Re_{\Delta}^{\min} N_{bl}/(Re_x - (Re_{\Delta}^{\min} N_{bl}/K)^{7/6})]$ , where  $Re_x$  is the Reynolds number based on the distance to the leading-edge and  $K$  is a constant. The model errors are included in Figure 19(d) (dashed lines), and provide a reasonable explanation of the trends obtained from WMLES.

Although not shown, a power law approximation of  $\varepsilon_u$  in the range of  $Re_{\Delta}^{\min}$  considered in Figure 19(d) shows that the WMLES predictions approach the experimental solution as  $(Re_{\Delta}^{\min})^{\alpha}$ , with  $\alpha \approx 1 - 2$ . These local convergence rates are steeper than those for  $N_{bl}$  reported in the section above. Considering that the dependence of the total number of grid points is also milder for  $Re_{\Delta}^{\min}$  (i.e.,  $N_{\text{points}} \sim (Re_{\Delta}^{\min})^{-5/6}$ ) than for  $N_{bl}$  ( $N_{\text{points}} \sim N_{bl}^{13/6}$ ), the scaling of the grid resolution requirements for the leading-edge region is less demanding than the resolution to resolve the remaining turbulent boundary layers.

An important caveat of the present setup is that both the experiment and WMLES calculations were tripped at the leading-edge of the wing. This prevent us from evaluating the grid limitations in the presence of untripped laminar-to-turbulent transition. A second remark is that our analysis was conducted at a low angle of attack, and different conclusions might hold at higher values. In particular, investigations on a NACA 0012 [70] have shown that the flow prediction along the whole chord of the airfoil could be dramatically affected by the grid resolution details at the leading-edge. Our results do not display this sensitivity and our model does not account for the possibility of such drastic changes.

## E. Pressure coefficient

The surface pressure coefficient along the chord of the wing is shown in Figure 20. The predictions are compared with experimental data at four different  $y$ -locations denoted by the red lines in Figure 20(f). The error in  $C_p$  is quantified in Figure 21 as function of  $\Delta/\delta_c$ , where  $\delta_c$  is the averaged  $\delta$  along the  $x$  direction. Overall, WMLES agrees with the experimental data to within 1–5% error. The predictions remain to within 5% accuracy even when the boundary layers are marginally resolved (i.e., 0–1 points per  $\delta$ ). The accurate prediction of  $C_p$  along the main wing is a common observation in CFD of external aerodynamic applications with attached flows. As discussed in §IV, the result can be attributed to the inviscid nature of the mean pressure. Under the thin boundary layer approximation, the inviscid

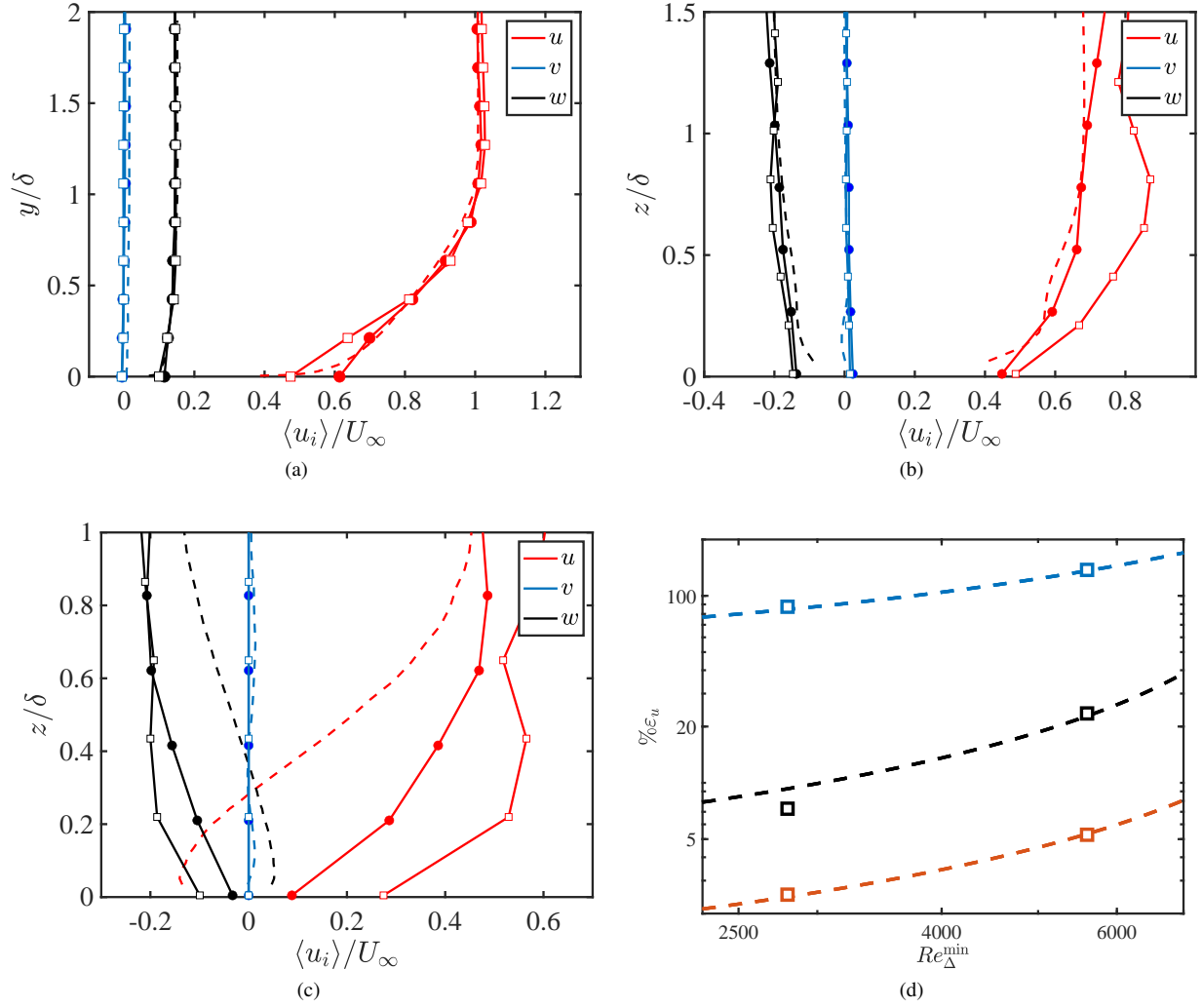


**Fig. 19** (a) Mean velocity profiles at (a) the fuselage region, (b) juncture region, and (c) separation zone for case C-N5-R2e3 ( $\circ$ ) and C-N5-R5e3 ( $\square$ ). Colors denote different velocity components. Experiments are denoted by dashed lines. The wall-normal distance is normalized by the local boundary-layer thickness  $\delta$  at the respective location. (d) Errors in the mean velocity profile (symbols) as a function of  $Re_{\Delta}^{\min}$  at the three locations shown in Figure 11 using the same color code: red (fuselage), black (juncture), and blue (separation). The dashed lines are proportional to  $\epsilon_u \sim 1/N_{bl}[1 + \Gamma Re_{\Delta}^{\min} N_{bl}/(Re_x - (Re_{\Delta}^{\min} N_{bl}/K)^{7/6})]$ , with  $Re_x$  the leading-edge Reynolds number,  $\Gamma = 300$ , and  $K = 0.16$ .

outer-flow pressure is directly imposed on the wall, which makes  $C_p$  relatively insensitive to the details of the near-wall turbulence. This is demonstrated by performing an additional inviscid calculation similar to C-D2 but imposing the free-slip boundary condition at the wall such that boundary layers are unable to develop (Figure 20(e)). The  $C_p$  for the case with free-slip wall is strikingly similar to its wall-modeled counterpart, confirming that  $C_p$  is dominated by inviscid contributions. The results also support the error analysis in §IV, where it was argued that errors in  $C_p$  of the form  $\varepsilon_p = \beta_p (\Delta/\delta)^{\alpha_p}$  should have  $\beta_p \ll 1$  and  $\alpha_p \approx 0$ .

The main discrepancies with experiments are at the leading edge and wing tip. The conditions for the thin boundary-layer approximation require the wall radius of curvature to be much larger than the boundary-layer thickness. This requirement might be satisfied to a lower degree in the vicinity of the wing leading-edge, which explains the slightly poorer predictions and higher sensitivity to  $\Delta$  in that region. The tripping methodology used in WMLES differs from the experimental setup, which may also contribute to the discrepancies observed with experiments at the leading edge. The inviscid assumption for  $C_p$  would not hold in the wing tip region due to the formation of the wing tip vortex by viscous roll-up. This is corroborated in Figure 20(d), which shows that WMLES underpredicts the  $C_p$  at the trailing edge of the wing tip with high sensitivity to the grid resolution. Figure 21(b) further reveals that the errors at the wing tip follow a linear relation,  $\varepsilon_p \sim (\Delta/\delta_c)$ . The best  $C_p$  prediction at the wing tip is attained by case C-N10-R2e3, which supports the strongest vortex core at the trailing edge as evidenced by the largest value of  $-C_p$ . By construction, BL-conforming grids are designed to cluster points in those regions where viscous effects are important (see Section III.A). In the case of the wing tip, the equalization of the top and bottom pressure of the wing results in a crossflow boundary-layer that is effectively captured by BL-conforming grids, and this in turn permits the formation of stronger and more realistic wing tip vortices.

Overall, the outer-flow nature of  $C_p$  is encouraging for the prediction of the pressure-induced components of the lift and drag coefficients. Our results, like previous studies in the literature, suggest that  $C_p$  might not be a particularly challenging quantity to predict in the presence of wall-attached boundary layers (for example, over the main body of the wing at low angles of attack). Hence, efforts should be devoted to improving the predictions at the leading edge and wing tips, and to predict other viscous-dominated quantities such as the skin-friction coefficient.

## F. Visualization of the separation bubble

The mean wall-stress streamlines for case C-D0.5 are shown in Figure 22. The figure also contains a depiction of the average length and width of the separation bubble, which are about 100 mm and 60 mm, respectively, for case C-D0.5. Direct comparison of these dimensions with oil-film experimental results show that the WMLES prediction is about 15% lower than the experimental measurements ( $120 \times 80$  mm), consistent with previous WMLES investigations [26–28]. Nonetheless, it is important to note that the sizes of the separation bubble from WMLES are calculated from the time-average tangential wall-stress streamlines, whereas the experimental sizes are obtained from the pattern resulting

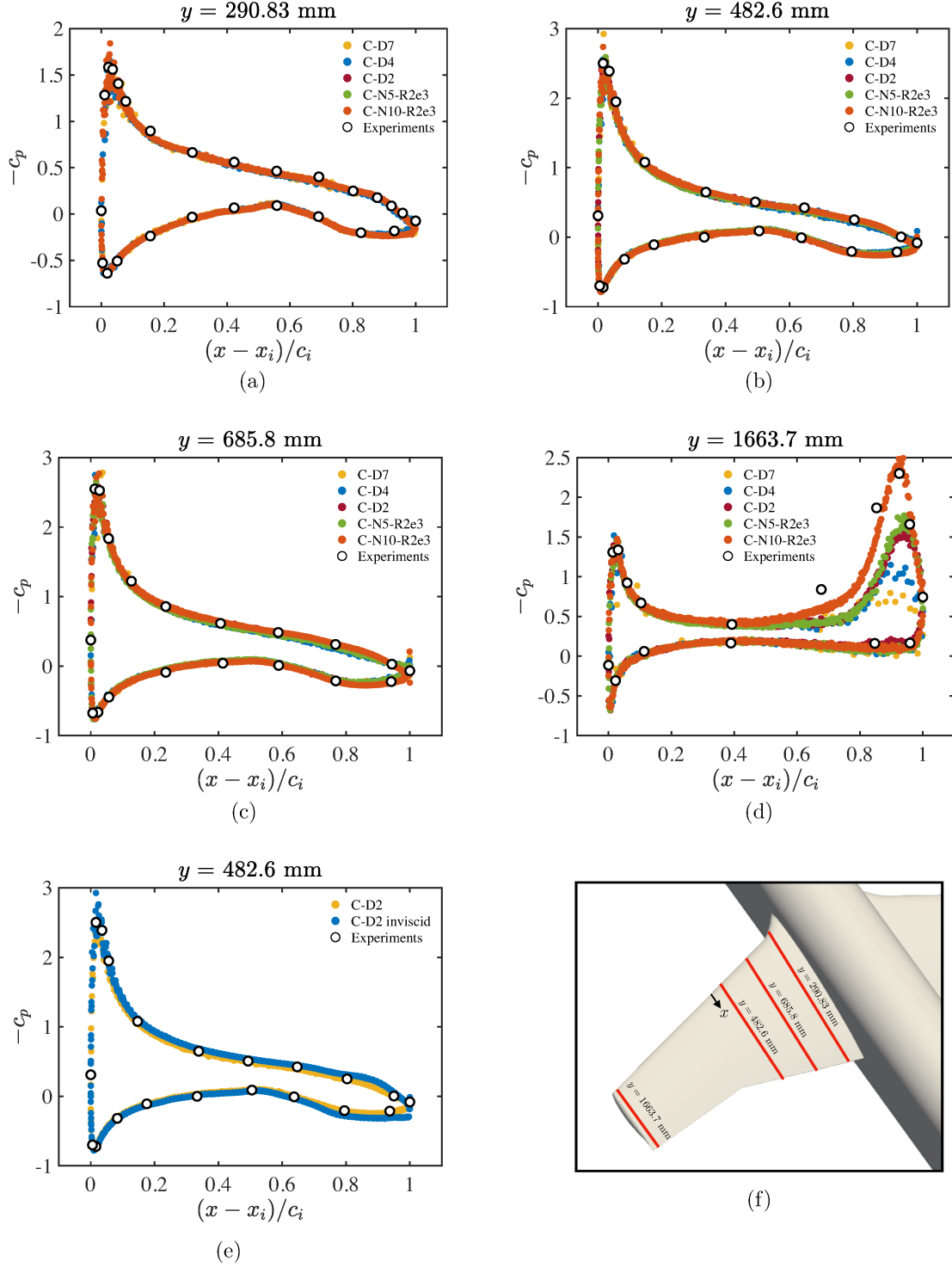


**Fig. 20** The surface pressure coefficient  $C_p$  along the wing normalized by the local chord  $c_i$  and with respect to the local leading-edge coordinate  $x_i$ . Panels (a), (b), (c) and (d) show  $C_p$  for cases C-D7, C-D4, C-D2, C-N5-R2e3, and C-N10-R2e3 at different  $y$  locations. Panel (e) shows  $C_p$  for case C-D2 and a case identical to C-D2 but imposing free-slip boundary condition at the walls. (f) Locations over the wing selected to plot  $C_p$  in panels (a), (b), (c), (d) and (e).

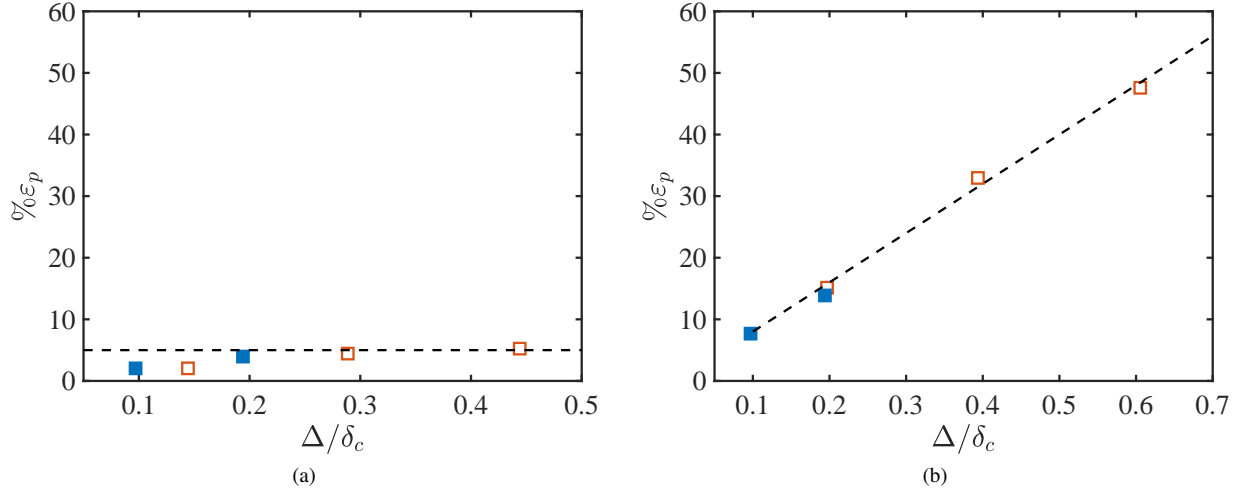


**Fig. 21** Errors in the surface pressure coefficient at (a)  $y = 482.6$  mm (close to the crank chord) and (b)  $y = 1663.7$  mm (wing tip) as a function of  $\Delta/\delta_c$ , where  $\delta_c$  is the averaged  $\delta$  along the streamwise direction of the station considered. The black dashed line in panel (a) is  $\varepsilon_p = 5\%$  and in panel (b)  $\varepsilon_p \sim \Delta/\delta_c$ .

from the temporal evolution of the oil film. Albeit both methodologies provide an average description of the size of the separation zone, they do not allow for one to one comparisons and we should not interpret the present differences as a faithful quantification of the errors.

## VI. Conclusions

We have investigated the cost and error scaling of WMLES for external aerodynamic applications. The NASA Juncture Flow was selected as representative of an aircraft with trailing-edge smooth-body separation. The simulations were conducted using charLES with Voronoi grids at an angle of attack of  $5^\circ$  and  $Re = 2.4 \times 10^6$ . Two gridding strategies have been examined: i) constant-size grid, in which the near-wall grid size has a constant value and ii) boundary-layer-conforming grid (BL-conforming grid), in which the grid size varies to accommodate the growth of the boundary-layer thickness  $\delta$ . In the latter, the boundary-layer thickness was estimated by the difference between the solution of WMLES and an inviscid calculation. BL-conforming grids are characterized by  $N_{bl}$  (number of points per  $\delta$ ) and  $Re_{\Delta}^{\min}$  (minimum grid-size Reynolds number), and their cost in terms of the number of control volume scales roughly as  $N_{bl}^{13/6} Re (Re_{\Delta}^{\min})^{-5/6}$ . This implies that the cost of WMLES grows as  $N_{bl}^{13/6} \approx N_{bl}^2$ , and from there the critical importance of assessing the minimum value of  $N_{bl}$  required to attain the desired accuracy in the quantities of interest.

We have focused on the prediction of the mean velocity profile and the surface pressure coefficient  $C_p$ . Our analysis was accompanied by theoretical estimations of the error in a zero-pressure gradient turbulent boundary layer (ZPGTBL), which was used as the baseline to assess the performance of WMLES in the NASA Juncture Flow. From a theoretical viewpoint, the errors in the  $C_p$  are expected to be low and mostly grid independent at regions where the thin boundary



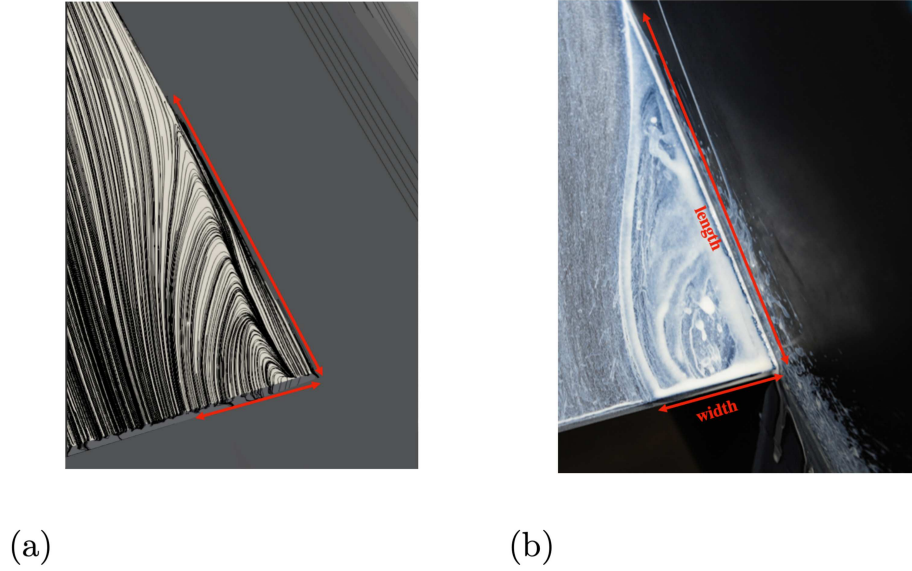


**Fig. 22 (a) Streamlines of the average tangential wall-stress for C-D0.5. (b) Experimental oil-film visualization.**

layer approximation holds. For the mean velocity profile, the errors should scale linearly with the grid size for flows resembling a ZPGTBL. We have also distinguished two types of wall-modeling errors: internal errors, due to the limitations of the wall model to represent the near-wall turbulence (e.g., law of the wall); and external errors, which originate from the outer LES solution.

Three different locations were considered to investigate the errors in the mean velocity profile: the upstream region of the fuselage, the wing-body juncture, and the wing-body juncture close to the trailing-edge. The last two locations are characterized by strong mean-flow three-dimensionality and separation. A summary of the errors incurred by WMLES in predicting mean velocity profiles is shown in Figure 17(a). The message conveyed by the results is that WMLES performs as expected in regions where the flow resembles a zero-pressure-gradient turbulent boundary layer, consistent with our theoretical predictions. However, there is a decline of the current models in the presence of wing-body junctions and, more acutely, in separated zones. These errors are mitigated by the use of BL-conforming grids, which enable a more efficient distribution of grid points across the boundary layer. It was argued that the improved accuracy provided by BL-conforming is related to the reduced propagation of WMLES errors along the streamwise direction of the flow. Nonetheless, the errors in the juncture and separated region exhibit slow convergence rates regardless of the grid strategy, rendering the brute-force grid-refinement approach too costly as a pathway to improve the accuracy of the solution. The

results reported above for the mean velocity profile converge monotonically to the experimental solution. However, we have shown that WMLES can exhibit a non-monotonic convergence for some intermediate grid resolutions in the range  $\Delta \approx 0.03 - 0.05\delta$ , which might pose an additional challenge to the robustness and reliability of WMLES.

The impact on the solution of the errors from the underresolved leading-edge was also analyzed using BL-conforming grids. The leading-edge grid resolution was controlled by the parameter  $Re_{\Delta}^{\min}$ . In first order approximation, the leading-edge errors decay linearly with the streamwise distance to the underresolved leading-edge. However, these errors can still propagate downstream for long distances, deteriorating the quality of the solution even at the wing trailing-edge. In spite of that, the convergence rate of the solution for decreasing  $Re_{\Delta}^{\min}$  suggests that the leading-edge grid resolution might be less demanding than the grid resolution required to resolve the subsequent turbulent boundary layers. Our study is limited to low angles of attack and different conclusions might hold at higher values, especially involving flow separation and stall. In addition, the Juncture Flow Experiment and our simulations are both tripped close to the leading-edge, which may also bias our observations.

The errors in the mean pressure coefficient were assessed at four spanwise locations ranging from the fuselage to the wing tip. The prediction of  $C_p$  in the main wing is below 5% error for all grid sizes considered, even when boundary layers were marginally resolved. This high accuracy can be attributed to the inviscid nature of the mean pressure, which makes  $C_p$  insensitive to flow details within the turbulent boundary layer. The most challenging locations for WMLES are the leading edge and wing tip, where the inviscid assumption breaks down. Similarly to the mean velocity profile, BL-conforming grids deliver higher accuracy in the prediction of  $C_p$  at the wing tip with a lower computational cost.

Other relevant quantities of interest not investigated here include the pointwise mean stress at the wall, and integrated quantities such as lift, drag and moment coefficients, the last three being particularly important for engineering applications. Unfortunately, the pointwise friction coefficient is not available from the experimental campaign of the NASA Juncture Flow, which hinders our ability to assess the performance of the wall models more thoroughly. We also lack information on the lift, drag and moment coefficients, and the impact of the modeling deficiencies identified above on these quantities remains uncertain at this point.

The results presented here highlight the benefits of BL-conforming grids in terms of accuracy and computational cost. Nevertheless, we have also identified several outstanding issues that remain to be solved. Among them, we can cite the decline in performance of current modeling approaches in separated regions and corner flows, the non-monotonic convergence of WMLES, and the necessity of acquiring richer experimental measurements (such as pointwise skin friction coefficient) to assess and aid the development of models.

## Acknowledgments

This work was supported by NASA under grant No. NNX15AU93A. The authors also acknowledge the computational resources provided by the NASA High-End Computing (HEC) Program through the NASA Advanced Supercomputing

(NAS) Division at Ames Research Center. A.L.-D. acknowledges the MIT SuperCloud and Lincoln Laboratory Supercomputing Center for providing HPC resources that have contributed to the research results reported within this work. We thank Jane Bae and Konrad Goc for helpful comments. We are also thankful to Michael Emory from Cascade Technologies, Inc. for his guidance on grid generation.

## Appendix A: Grid point count of BL-conforming grids in ZPGTBL

Let us consider a ZPGTBL over a flat plate of streamwise length  $L_x$  spanwise width  $L_z$ , and leading edge at  $x = 0$ . We aim at calculating the number of grid points required for WMLES using BL-conforming grids with  $N_{bl}$  and  $Re_{\Delta}^{\min}$ . An schematic of the distribution of grid points was shown in Figure 3(b). The grid resolution at a given  $x$  is  $\Delta(x) = \delta(x)/N_{bl}$  for  $\delta > \delta_{\min} = \Delta_{\min}N_{bl}$ . Once the boundary layer thickness is below  $\delta_{\min}$ , the grid resolution is kept constant to  $\Delta_{\min}$ . The number of grid points can be divided into points at the leading edge  $N_{LE}$  and the rest  $N_R$ . Assuming a fully turbulent boundary layer growing as  $\delta/x = K Re_x^{-1/7}$  with  $Re_x = xU_{\infty}/\nu$  and  $K = 0.16$ , the number of grid points is

$$N_{\text{points}} = N_{LE} + N_R = \frac{L_z N_{bl}^{13/6}}{L_x K^{7/6}} \frac{Re}{(Re_{\Delta}^{\min})^{5/6}} + \frac{7}{5} \frac{L_z N_{bl}^{13/6}}{L_x K^{7/6}} \frac{Re}{(Re_{\Delta}^{\min})^{5/6}} \left( 1 - \frac{(N_{bl} Re_{\Delta}^{\min}/K)^{5/6}}{Re^{5/7}} \right), \quad (13)$$

where  $Re = L_x U_{\infty}/\nu$ . Equation (13) shows that the number of grid points for BL-conforming grids scales as  $N_{bl}^{13/6} (Re_{\Delta}^{\min})^{5/6} Re$ , which is exact for ZPGTBL with  $\delta$  following the 1/7-th growth law. In the case of the NASA Juncture Flow, the value of  $N_{\text{points}}$  differs from Eq. (13) (as seen in figure 6) due to deviations in  $\delta$  from a ZPGTBL and the geometric complexities of the aircraft surface, which makes  $\Delta$  a function of the two wall-parallel directions. Nonetheless, Eq. (13) offers a simple model to rationalize the scaling of the cost of flow simulations for an aircraft-like geometry dominated by attached boundary layers.

We have characterized the quality of BL-conforming grids as a function of  $N_{bl}$  and  $Re_{\Delta}^{\min}$ , where the latter is a measure of the leading-edge resolution. An advantage of using  $Re_{\Delta}^{\min}$  is that it grants direct control over the minimum grid size  $\Delta_{\min}$ . However, the streamwise extent of the underresolved leading-edge region ( $L_0$  at which  $\delta = \delta_{\min}$ , Figure 3b) will change with varying  $N_{bl}$  even if  $Re_{\Delta}^{\min}$  is held constant. This can be seen from the relation  $L_0/L_x = (Re_{\Delta}^{\min} N_{bl}/K)^{7/6} Re^{-1}$ . To avoid changes in  $L_0$  with  $N_{bl}$ , an alternative approach is to replace  $Re_{\Delta}^{\min}$  by the underresolved leading-edge Reynolds number  $Re_{L_0} = U_{\infty} L_0/\nu$ . The price to pay for using  $Re_{L_0}$  instead of  $Re_{\Delta}^{\min}$  is the lack of direct control over  $\Delta_{\min}$  and the complexities of calculating  $L_0$  in the actual geometry. The number of grid points to resolve a flat plate as a function of  $N_{bl}$  and  $Re_{L_0}$  is now given by

$$N_{\text{points}} = N_{LE} + N_R = \frac{L_z N_{bl}^3}{L_x K^2} \frac{Re}{Re_{L_0}^{5/7}} + \frac{7}{5} \frac{L_z N_{bl}^3}{L_x K^2} \frac{Re}{Re_{L_0}^{5/7}} \left( 1 - \left( \frac{Re_{L_0}}{Re} \right)^{5/7} \right), \quad (14)$$

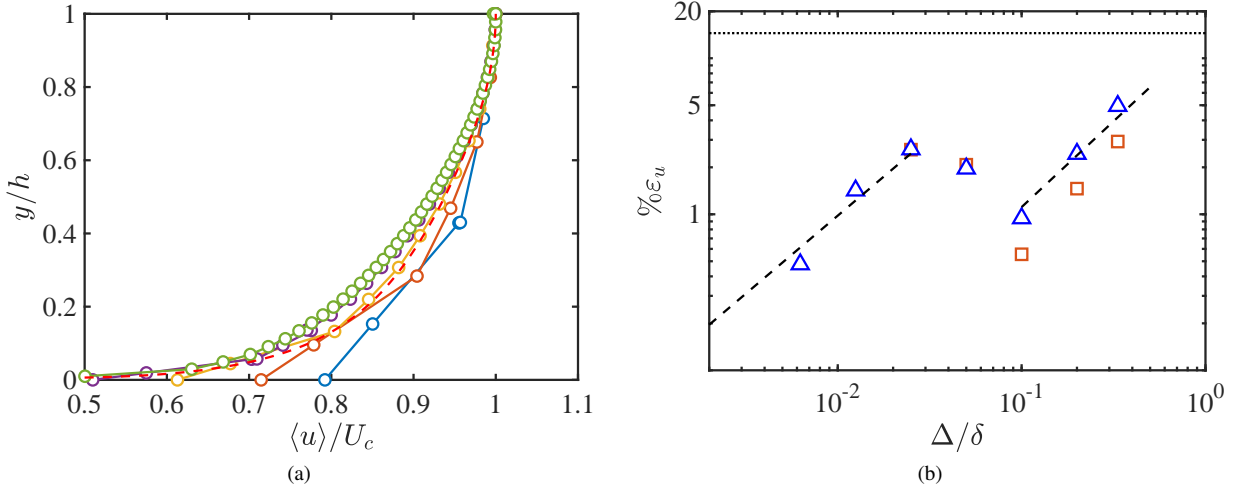


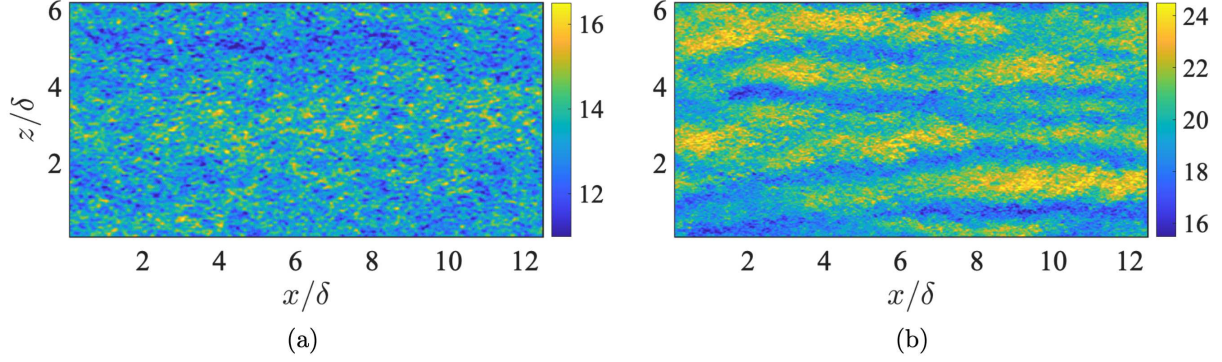
**Fig. 23** (a) The mean velocity profile for WMLES with charLES of a turbulent channel flow. The colors denote different grid resolutions from coarser to finer: blue, red, yellow, purple, and green. (b) Error in the mean velocity profile  $\varepsilon_u$  as a function of the grid resolution  $\Delta$  for WMLES of turbulent channel flow. The symbols denote simulations using charLES with Voronoi grids ( $\square$ , red) and finite-difference solver with staggered grids ( $\triangle$ , blue). The dashed line is  $\varepsilon_u \sim \Delta/\delta$ . The horizontal dotted line is the error from the inviscid solution.

which shows that the new expected cost scales as  $N_{\text{bl}}^3 Re_{L_0}^{-5/7} Re$ . The modification of the cost scaling law for WMLES with the selection of either  $Re_{\Delta}^{\min}$  or  $Re_{L_0}$  should come as no surprise, as each choice constitutes a different grid strategy. In this work, we have favored  $Re_{\Delta}^{\min}$  due to its simplicity. Nonetheless, other parametrizations, such as  $Re_{L_0}$ , might also provide acceptable descriptions of the leading-edge grid resolution.

## Appendix B: Non-monotonic convergence of WMLES

The purpose of this appendix is to document more thoroughly the convergence of WMLES in turbulent channel flows using charLES with Voronoi isotropic grids. The friction Reynolds number is set to  $Re_{\tau} = 4200$  and seven grid resolutions are considered:  $\Delta/\delta = 1/3, 1/5, 1/10, 1/20, 1/40, 1/80$  and  $1/160$ . The last four grid sizes are finer than ones we could afford for the Juncture Flow Experiment. To assess the effect of the numerical scheme and gridding strategy, the results are compared with the error obtained from WMLES of turbulent channel flows using the finite-difference solver with staggered grid from Lozano-Durán and Bae [71], Lozano-Durán et al. [72]. All the simulations are conducted with dynamic Smagorinsky model and the equilibrium wall model. The channels are driven by holding the centerline velocity  $U_c$  to a constant value. Figure 23(a) contains the mean velocity profiles obtained with charLES for the all the grid resolutions considered. The error in the mean velocity profile is reported in figure 23(b) as a function of  $\Delta$ . The results show a non-monotonic convergence of  $\varepsilon_u$  and errors from both solvers deviate from  $\varepsilon_u \sim \Delta$  for  $\Delta/\delta \approx 0.03$ – $0.05$ . The linear trend is recovered again for  $\Delta/\delta < 0.03$ .

The non-monotonic convergence of the mean velocity profile was also observed by Lozano-Durán and Bae [61].



Instantaneous streamwise velocity in a turbulent channel flow at the wall-parallel plane  $y = 0.3\delta$ . The simulations are performed using charLES without SGS model with grid resolutions of (a)  $\Delta = 0.05\delta$  and (b)  $\Delta = 0.025\delta$ . The latter case is able to support streaky velocity structures even in the absence of explicit SGS model.

**Fig. 24**

They argued that this behavior can be traced back to the ability of the LES grid to support streamwise velocity streaks in the absence of SGS model. To test this idea, we repeat the simulations in charLES without an explicit SGS model, i.e., the numerical truncation errors act as the SGS model. To avoid any errors from the wall model, the equilibrium wall models is replaced by an exact wall-stress boundary condition in which the mean wall stress from DNS is directly imposed at the walls. Visual inspection of the instantaneous streamwise velocity for cases without SGS model in figure 24 shows that there is a substantial change in the flow structure at the critical grid size  $\Delta_c/\delta \approx 0.03\text{--}0.05$ . For  $\Delta > \Delta_c$ , the streamwise velocity lacks the characteristic features from wall turbulence and exhibits instead a highly noisy structure (figure 24(a)), as expected for LES in coarse grids without an explicit SGS model. On the other hand, a clearly defined streaky structure emerges for  $\Delta < \Delta_c$  (figure 24(b)), even in the absence of SGS model. We can hypothesize that the transition observed at  $\Delta_c$  will also take place in the presence of an explicit SGS model, causing the non-monotonic convergence of  $\varepsilon_u$  reported in figure 23(b). Note that the flow transition observed at  $\Delta_c$  is independent of wall modeling errors, as the simulations were performed by imposing the mean exact wall stress from DNS. In actual WMLES, the underperformance of the SGS model will propagate to the wall model via external errors as discussed in §IV. It is interesting that the critical grid resolution  $\Delta_c$  is roughly the same for the two solvers considered despite the fact that they comprise different numerical schemes and grid strategies. The latter observation points to a physical origin of  $\Delta_c$  in the sense that its value is dictated by physical constraints rather than by the numerical details of the solver, at least for low dissipation and energy preserving numerical schemes. Indeed, Lozano-Durán and Bae [61] showed that the grid resolution to resolve 90% of the turbulent kinetic energy is  $\Delta_{\min} \approx 0.04\delta$  at  $y \approx 0.5\delta$ , that is roughly equal to  $\Delta_c$ . Although the results here provide some insight into the origin of the non-monotonic convergence of WMLES, we still lack a satisfactory explanation of the phenomenon and, more importantly, a robust remedy.

## References

- [1] Johnson, F. T., Tinoco, E. N., and Yu, N. J., “Thirty years of development and application of CFD at Boeing Commercial Airplanes, Seattle,” *Computers & Fluids*, Vol. 34, No. 10, 2005, pp. 1115–1151.
- [2] Abbas-Bayoumi, A., and Becker, K., “An industrial view on numerical simulation for aircraft aerodynamic design,” *Journal of Mathematics in Industry*, Vol. 1, No. 1, 2011, pp. 1–14.
- [3] Spalart, P. R., and Venkatakrishnan, V., “On the role and challenges of CFD in the aerospace industry,” *The Aeronautical Journal*, Vol. 120, No. 1223, 2016, pp. 209–232. <https://doi.org/10.1017/aer.2015.10>.
- [4] Clark, A. M., Slotnick, J. P., Taylor, N. J., and Rumsey, C. L., “Requirements and challenges for CFD validation within the High-Lift Common Research Model ecosystem,” *AIAA Aviation Forum*, 2020. <https://doi.org/10.2514/6.2020-2772>, URL <https://arc.aiaa.org/doi/abs/10.2514/6.2020-2772>.
- [5] *Recommended Practice: When Flight Modelling Is Used to Reduce Flight Testing Supporting Aircraft Certification (AIAA R-154-2021)*, 2021.
- [6] Slotnick, J., Khodadoust, A., Alonso, J., Darmofal, D., Gropp, W., Lurie, E., and Mavriplis, D., *CFD Vision 2030 Study: A Path to Revolutionary Computational Aerosciences*, Tech. Rep. CR–2014-218178, NASA, 2014.
- [7] Rumsey, C. L., Carlson, J., and Ahmad, N., “FUN3D Juncture Flow computations compared with experimental data,” *AIAA Scitech Forum*, 2019. <https://doi.org/10.2514/6.2019-0079>.
- [8] Witherden, F. D., and Jameson, A., *Future Directions in Computational Fluid Dynamics*, 2017. <https://doi.org/10.2514/6.2017-3791>, URL <https://arc.aiaa.org/doi/abs/10.2514/6.2017-3791>.
- [9] Cho, M., Lozano-Durán, A., Moin, P., and Ilhwan Park, G., “Wall-Modeled Large-Eddy Simulation of Turbulent Boundary Layers with Mean-Flow Three-Dimensionality,” *AIAA Journal*, Vol. 59, No. 5, 2021, pp. 1707–1717. <https://doi.org/10.2514/1.J059861>.
- [10] Rumsey, C. L., Slotnick, J. P., and Sclafani, A. J., *Overview and Summary of the Third AIAA High Lift Prediction Workshop*, 2018. <https://doi.org/10.2514/6.2018-1258>, URL <https://arc.aiaa.org/doi/abs/10.2514/6.2018-1258>.
- [11] Rumsey, C. L., and Ying, S. X., “Prediction of high lift: review of present CFD capability,” *Progress in Aerospace Sciences*, Vol. 38, No. 2, 2002, pp. 145–180. [https://doi.org/https://doi.org/10.1016/S0376-0421\(02\)00003-9](https://doi.org/https://doi.org/10.1016/S0376-0421(02)00003-9), URL <https://www.sciencedirect.com/science/article/pii/S0376042102000039>.
- [12] Vassberg, J. C., Tinoco, E. N., Mani, M., Brodersen, O. P., Eisfeld, B., Wahls, R. A., Morrison, J. H., Zickuhr, T., Laflin, K. R., and Mavriplis, D. J., “Abridged Summary of the Third AIAA Computational Fluid Dynamics Drag Prediction Workshop,” *J. Aircr.*, Vol. 45, No. 3, 2008, pp. 781–798. <https://doi.org/10.2514/1.30572>.
- [13] Rumsey, C. L., and Morrison, J. H., “Goals and Status of the NASA Juncture Flow Experiment,” *NATO STO*, 2016.
- [14] Rumsey, C. L., Neuhart, D., and Kegerise, M. A., “The NASA Juncture Flow Experiment: goals, progress, and preliminary testing (Invited),” *54th AIAA Aerospace Sciences Meeting*, 2016. <https://doi.org/10.2514/6.2016-1557>.

- [15] Kegerise, M. A., Neuhart, D., Hannon, J., and Rumsey, C. L., “An Experimental Investigation of a Wing-Fuselage Junction Model in the NASA Langley 14- by 22-Foot Subsonic Wind Tunnel,” *AIAA Scitech Forum*, 2019. <https://doi.org/10.2514/6.2019-0077>.
- [16] Rumsey, C. L., “The NASA Juncture Flow Test as a model for effective CFD/experimental collaboration,” *AIAA Applied Aerodynamics Conference*, 2018. <https://doi.org/10.2514/6.2018-3319>.
- [17] Lee, H. C., Pulliam, T. H., Neuhart, D., and Kegerise, M. A., “CFD analysis in advance of the NASA Juncture Flow Experiment,” *47th AIAA Fluid Dynamics Conference*, 2017. <https://doi.org/10.2514/6.2017-4127>.
- [18] Lee, H., Pulliam, T., Rumsey, C., and Carlson, J.-R., “Simulations of the NASA Langley 14-by 22-Foot Subsonic Tunnel for the Juncture Flow Experiment,” *NATO STO*, 2018.
- [19] Anderson, W., and Bonhaus, D. L., “An implicit upwind algorithm for computing turbulent flows on unstructured grids,” *Computers & Fluids*, Vol. 23, No. 1, 1994, pp. 1–21. [https://doi.org/https://doi.org/10.1016/0045-7930\(94\)90023-X](https://doi.org/https://doi.org/10.1016/0045-7930(94)90023-X), URL <https://www.sciencedirect.com/science/article/pii/004579309490023X>.
- [20] Anderson, W., Rausch, R. D., and Bonhaus, D. L., “Implicit/Multigrid Algorithms for Incompressible Turbulent Flows on Unstructured Grids,” *J. Comput. Phys.*, Vol. 128, No. 2, 1996, pp. 391–408. <https://doi.org/10.1006/jcph.1996.0219>, URL <https://doi.org/10.1006/jcph.1996.0219>.
- [21] Anderson, W. K., and Bonhaus, D. L., “Airfoil design on unstructured grids for turbulent flows,” *AIAA journal*, Vol. 37, No. 2, 1999, pp. 185–191.
- [22] Lee, H. C., and Pulliam, T. H., “Overflow Juncture Flow Computations Compared with Experimental Data,” *AIAA Scitech Forum*, 2019. <https://doi.org/10.2514/6.2019-0080>.
- [23] Spalart, P. R., Jou, W. H., Strelets, M., Allmaras, S. R., et al., “Comments on the feasibility of LES for wings, and on a hybrid RANS/LES approach,” *Advances in DNS/LES*, Vol. 1, 1997, pp. 4–8.
- [24] Spalart, P. R., “Detached-eddy simulation,” *Annu. Rev. Fluid Mech.*, Vol. 41, 2009, pp. 181–202.
- [25] Bose, S. T., and Park, G. I., “Wall-modeled large-eddy simulation for complex turbulent flows,” *Annu. Rev. Fluid Mech.*, Vol. 50, 2018, pp. 535–561.
- [26] Iyer, P. S., and Malik, M. R., “Wall-modeled LES of the NASA Juncture Flow Experiment,” *AIAA Scitech Forum*, 2020. <https://doi.org/10.2514/6.2020-1307>, URL <https://arc.aiaa.org/doi/abs/10.2514/6.2020-1307>.
- [27] Ghate, A. S., Housman, J. A., Stich, G.-D., Kenway, G., and Kiris, C. C., “Scale Resolving Simulations of the NASA Juncture Flow Model using the LAVA Solver,” *AIAA Aviation Forum*, 2020. <https://doi.org/10.2514/6.2020-2735>, URL <https://arc.aiaa.org/doi/abs/10.2514/6.2020-2735>.
- [28] Lozano-Durán, A., Bose, S. T., and Moin, P., “Prediction of trailing edge separation on the NASA Juncture Flow using wall-modeled LES,” *AIAA Scitech Forum*, 2020. <https://doi.org/10.2514/6.2020-1776>, URL <https://arc.aiaa.org/doi/abs/10.2514/6.2020-1776>.

- [29] Lozano-Durán, A., Bose, S. T., and Moin, P., “Performance of wall-modeled LES for external aerodynamics in the NASA Juncture Flow,” *Center for Turbulence Research - Annual Research Briefs*, 2020, pp. 33–48.
- [30] Piomelli, U., and Balaras, E., “Wall-layer models for large-eddy simulations,” *Annu. Rev. Fluid Mech.*, Vol. 34, 2002, pp. 349–374. <https://doi.org/10.1146/annurev.fluid.34.082901.144919>.
- [31] Cabot, W. H., and Moin, P., “Approximate wall boundary conditions in the large-eddy simulation of high Reynolds number flow,” *Flow Turbul. Combust.*, Vol. 63, 2000, pp. 269–291. <https://doi.org/10.1023/A:1009958917113>.
- [32] Larsson, J., Kawai, S., Bodart, J., and Bermejo-Moreno, I., “Large eddy simulation with modeled wall-stress: recent progress and future directions,” *Mech. Eng. Rev.*, Vol. 3, No. 1, 2016, pp. 1–23. <https://doi.org/10.1299/mer.15-00418>.
- [33] Deardorff, J., “A numerical study of three-dimensional turbulent channel flow at large Reynolds numbers,” *J. Fluid Mech.*, Vol. 41, No. 1970, 1970, pp. 453–480.
- [34] Schumann, U., “Subgrid scale model for finite difference simulations of turbulent flows in plane channels and annuli,” *J. Comp. Phys.*, Vol. 18, 1975, pp. 376–404. [https://doi.org/10.1016/0021-9991\(75\)90093-5](https://doi.org/10.1016/0021-9991(75)90093-5).
- [35] Piomelli, U., Ferziger, J., Moin, P., and Kim, J., “New approximate boundary conditions for large eddy simulations of wall-bounded flows,” *Phys. Fluids A*, Vol. 1, No. 6, 1989, pp. 1061–1068. <https://doi.org/10.1063/1.857397>.
- [36] Balaras, E., Benocci, C., and Piomelli, U., “Two-layer approximate boundary conditions for large-eddy simulations,” *AIAA J.*, Vol. 34, No. 6, 1996, pp. 1111–1119. <https://doi.org/10.2514/3.13200>.
- [37] Wang, M., and Moin, P., “Dynamic wall modeling for large-eddy simulation of complex turbulent flows,” *Phys. Fluids*, Vol. 14, No. 7, 2002, pp. 2043–2051.
- [38] Chung, D., and Pullin, D. I., “Large-eddy simulation and wall modelling of turbulent channel flow,” *J. Fluid Mech.*, Vol. 631, 2009, pp. 281–309. <https://doi.org/10.1017/S0022112009006867>.
- [39] Bodart, J., and Larsson, J., “Wall-modeled large eddy simulation in complex geometries with application to high-lift devices,” *Center for Turbulence Research - Annual Research Briefs*, 2011, pp. 37–48.
- [40] Kawai, S., and Larsson, J., “Wall-modeling in large eddy simulation: Length scales, grid resolution, and accuracy,” *Phys. Fluids*, Vol. 24, No. 1, 2012, p. 015105. <https://doi.org/10.1063/1.3678331>.
- [41] Kawai, S., and Larsson, J., “Dynamic non-equilibrium wall-modeling for large eddy simulation at high Reynolds numbers,” *Phys. Fluids*, Vol. 25, No. 1, 2013, p. 015105.
- [42] Bermejo-Moreno, I., Campo, L., Larsson, J., Bodart, J., Helmer, D., and Eaton, J. K., “Confinement effects in shock wave/turbulent boundary layer interactions through wall-modelled large-eddy simulations,” *J. Fluid Mech.*, Vol. 758, 2014, pp. 5–62. <https://doi.org/10.1017/jfm.2014.505>.



- [43] Park, G. I., and Moin, P., “An improved dynamic non-equilibrium wall-model for large eddy simulation,” *Phys. Fluids*, Vol. 26, No. 1, 2014, p. 015108. <https://doi.org/10.1063/1.4861069>.
- [44] Yang, X. I. A., Sadique, J., Mittal, R., and Meneveau, C., “Integral wall model for large eddy simulations of wall-bounded turbulent flows,” *Phys. Fluids*, Vol. 27, No. 2, 2015, p. 025112. <https://doi.org/10.1063/1.4908072>.
- [45] Lozano-Durán, A., and Bae, H. J., “Self-critical machine-learning wall-modeled LES for external aerodynamics,” *Center for Turbulence Research - Annual Research Briefs*, 2020, pp. 197–210.
- [46] Poinso, T., and Lele, S., “Boundary conditions for direct simulations of compressible viscous flows,” *J. Comput. Phys.*, Vol. 101, No. 1, 1992, pp. 104 – 129. [https://doi.org/https://doi.org/10.1016/0021-9991\(92\)90046-2](https://doi.org/https://doi.org/10.1016/0021-9991(92)90046-2).
- [47] Bres, G. A., Bose, S. T., Emory, M., Ham, F. E., Schmidt, O. T., Rigas, G., and Colonius, T., “Large-eddy simulations of co-annular turbulent jet using a Voronoi-based mesh generation framework,” *2018 AIAA/CEAS Aeroacoustics Conference*, 2018, p. 3302.
- [48] Fu, L., Karp, M., Bose, S. T., Moin, P., and Urzay, J., “Shock-induced heating and transition to turbulence in a hypersonic boundary layer,” *J. Fluid Mech.*, Vol. 909, 2021, p. A8. <https://doi.org/10.1017/jfm.2020.935>.
- [49] Moin, P., Squires, K., Cabot, W., and Lee, S., “A dynamic subgrid-scale model for compressible turbulence and scalar transport,” *Phys. Fluids*, Vol. 3, No. 11, 1991, pp. 2746–2757. <https://doi.org/10.1063/1.858164>.
- [50] Lilly, D. K., “A proposed modification of the Germano subgrid-scale closure method,” *Phys. Fluids A*, Vol. 4, No. 3, 1992, pp. 633–635. <https://doi.org/10.1063/1.858280>.
- [51] Vinuesa, R., Bobke, A., Örlü, R., and Schlatter, P., “On determining characteristic length scales in pressure-gradient turbulent boundary layers,” *Phys. Fluids*, Vol. 28, No. 5, 2016, p. 055101. <https://doi.org/10.1063/1.4947532>.
- [52] Asada, K., and Kawai, S., “Large-eddy simulation of airfoil flow near stall condition at Reynolds number  $2.1 \times 10^6$ ,” *Phys. Fluids*, Vol. 30, No. 8, 2018, p. 085103. <https://doi.org/10.1063/1.5037278>.
- [53] Coleman, G. N., Rumsey, C. L., and Spalart, P. R., “Numerical study of turbulent separation bubbles with varying pressure gradient and Reynolds number,” *J. Fluid Mech.*, Vol. 847, 2018, pp. 28–70. <https://doi.org/10.1017/jfm.2018.257>.
- [54] Spalart, P. R., and Watmuff, J. H., “Experimental and numerical study of a turbulent boundary layer with pressure gradients,” *J. Fluid Mech.*, Vol. 249, 1993, pp. 337–371. <https://doi.org/10.1017/S002211209300120X>.
- [55] Uzun, A., and Malik, M. R., *Simulation of a Turbulent Flow Subjected to Favorable and Adverse Pressure Gradients, ????* <https://doi.org/10.2514/6.2020-3061>, URL <https://arc.aiaa.org/doi/abs/10.2514/6.2020-3061>.
- [56] Griffin, K. P., Fu, L., and Moin, P., “General method for determining the boundary layer thickness in nonequilibrium flows,” *Phys. Rev. Fluids*, Vol. 6, 2021, p. 024608. <https://doi.org/10.1103/PhysRevFluids.6.024608>, URL <https://link.aps.org/doi/10.1103/PhysRevFluids.6.024608>.

- [57] Chapman, D. R., “Computational aerodynamics development and outlook,” *AIAA J.*, Vol. 17, No. 12, 1979, pp. 1293–1313. <https://doi.org/10.2514/3.61311>.
- [58] Choi, H., and Moin, P., “Grid-point requirements for large eddy simulation: Chapman’s estimates revisited,” *Phys. Fluids*, Vol. 24, No. 1, 2012, p. 011702.
- [59] Yang, X. I. A., and Griffin, K. P., “Grid-point and time-step requirements for direct numerical simulation and large-eddy simulation,” *Phys. Fluids*, Vol. 33, No. 1, 2021, p. 015108. <https://doi.org/10.1063/5.0036515>.
- [60] Nagib, H. M., Chauhan, K. A., and Monkewitz, P. A., “Approach to an asymptotic state for zero pressure gradient turbulent boundary layers,” *Philosophical Transactions of the Royal Society A: Mathematical, Physical and Engineering Sciences*, Vol. 365, No. 1852, 2007, pp. 755–770. <https://doi.org/10.1098/rsta.2006.1948>, URL <https://royalsocietypublishing.org/doi/abs/10.1098/rsta.2006.1948>.
- [61] Lozano-Durán, A., and Bae, H. J., “Error scaling of large-eddy simulation in the outer region of wall-bounded turbulence,” *J. Comput. Phys.*, Vol. 392, 2019, pp. 532–555. <https://doi.org/10.1016/j.jcp.2019.04.063>.
- [62] Perry, A. E., and Abell, C. J., “Asymptotic similarity of turbulence structures in smooth- and rough-walled pipes,” *J. Fluid Mech.*, Vol. 79, 1977, pp. 785 – 799.
- [63] Jiménez, J., “Coherent structures in wall-bounded turbulence,” *J. Fluid Mech.*, Vol. 842, 2018, p. P1. <https://doi.org/10.1017/jfm.2018.144>.
- [64] Kolmogorov, A. N., “The Local Structure of Turbulence in Incompressible Viscous Fluid for Very Large Reynolds’ Numbers,” *Dokl. Akad. Nauk SSSR*, Vol. 30, 1941, pp. 301–305.
- [65] Lozano-Durán, A., and Jiménez, J., “Effect of the computational domain on direct simulations of turbulent channels up to  $Re_\tau = 4200$ ,” *Phys. Fluids*, Vol. 26, No. 1, 2014, p. 011702. <https://doi.org/10.1063/1.4862918>.
- [66] JCR, H., Wray, A., and Moin, P., “Eddies, stream, and convergence zones in turbulent flows,” *Center for turbulence research report CTR-S88*, 1988, pp. 193–208.
- [67] Winckelmans, G. S., Jeanmart, H., and Carati, D., “On the comparison of turbulence intensities from large-eddy simulation with those from experiment or direct numerical simulation,” *Physics of Fluids*, Vol. 14, No. 5, 2002, pp. 1809–1811. <https://doi.org/10.1063/1.1466824>.
- [68] Lozano-Durán, A., Giometto, M. G., Park, G. I., and Moin, P., “Non-equilibrium three-dimensional boundary layers at moderate Reynolds numbers,” *J. Fluid Mech.*, Vol. 883, 2020, p. A20. <https://doi.org/10.1017/jfm.2019.869>.
- [69] Sillero, J. A., Jiménez, J., and Moser, R. D., “One-point statistics for turbulent wall-bounded flows at Reynolds numbers up to  $\delta^+ \approx 2000$ ,” *Phys. Fluids*, Vol. 25, No. 10, 2013, p. 105102.
- [70] Goc, K., personal communication, 2021.

- [71] Lozano-Durán, A., and Bae, H. J., “Turbulent channel with slip boundaries as a benchmark for subgrid-scale models in LES,” *Center for Turbulence Research - Annual Research Briefs*, 2016, pp. 97–103.
- [72] Lozano-Durán, A., Hack, M. J. P., and Moin, P., “Modeling boundary-layer transition in direct and large-eddy simulations using parabolized stability equations,” *Phys. Rev. Fluids*, Vol. 3, 2018, p. 023901. <https://doi.org/10.1103/PhysRevFluids.3.023901>.